

# A decade of transit photometry for K2-19: Revised system architecture\*

J.M. Almenara<sup>ID 1, 2</sup>, R. Mardling<sup>ID 3, 1</sup>, A. Leleu<sup>ID 1</sup>, R.F. Díaz<sup>ID 4, 5</sup>, X. Bonfils<sup>ID 2</sup>, Ing-Guey Jiang<sup>ID 6</sup>, Li-Chin Yeh<sup>ID 7</sup>, Ming Yang<sup>ID 8</sup>, Keivan G. Stassun<sup>ID 9</sup>, Napaporn A-thano<sup>ID 10</sup>, Billy Edwards<sup>ID 11</sup>, F. Bouchy<sup>ID 1</sup>, V. Bourrier<sup>ID 1</sup>, A. Deline<sup>ID 1</sup>, D. Ehrenreich<sup>ID 1</sup>, E. Fontanet<sup>ID 1</sup>, T. Forveille<sup>ID 2</sup>, J.M. Jenkins<sup>ID 12</sup>, L.K.W. Kwok<sup>ID 1</sup>, M. Lendl<sup>ID 1</sup>, A. Psaridis<sup>ID 13, 14, 1</sup>, S. Udry<sup>ID 1</sup>, J. Venturini<sup>ID 1</sup>, and J. Winn<sup>ID 15</sup>

(Affiliations can be found after the references)

## ABSTRACT

The star K2-19 hosts a pair of Neptunian planets deep inside the 3:2 resonance. They induce strong transit-timing variations with two incommensurate frequencies. Previous photodynamical modeling of 3.3 years of transit and radial velocity data produced mass estimates of  $32.4 \pm 1.7 M_{\oplus}$  and  $10.8 \pm 0.6 M_{\oplus}$  for planets b and c, respectively, and corresponding eccentricity estimates of  $0.20 \pm 0.03$  and  $0.21 \pm 0.03$ . These high eccentricities raise questions about the formation origin of the system, and this motivated us to extend the observing baseline in an attempt to better constrain their values. We present a photodynamical analysis of 10 years of transit data that confirms the previous mass estimates ( $30.8 \pm 1.3 M_{\oplus}$  and  $11.1 \pm 0.4 M_{\oplus}$ ), but reduces the median eccentricities to  $0.04 \pm 0.02$  and  $0.07 \pm 0.02$  for b and c, respectively. These values are more consistent with standard formation models, but still involve nonzero free eccentricity. The previously reported high eccentricities appear to be due to a single transit for which measurements taken at twilight mimicked ingress. This resulted in a 12-minute error in the midtransit time. The data that covered 1.3 and 5 so-called super and resonant periods were used to match a Fourier analysis of the transit-timing variation signal with simple analytic expressions for the frequencies and amplitudes to obtain planet mass estimates within 2% of the median photodynamical values, regardless of the eccentricities. Theoretical details of the analysis are presented in a companion paper. Additionally, we identified a possible planet candidate situated exterior to the b–c pair. Finally, in contrast to a previous study, our internal structure modeling of K2-19 b yields a metal mass fraction that is consistent with core accretion.

**Key words.** stars: individual: K2-19 – stars: planetary systems – techniques: photometric

## 1. Introduction

The migration process is a complex mechanism that takes place in protoplanetary disks. It can result in the capture of planets in mean motion resonance (MMR) chains (Cresswell & Nelson 2008). When the protoplanetary disk dissipates, most of the resonant chains are expected to break (Izidoro et al. 2017; Dai et al. 2024) because most systems are observed outside the MMR (Fabrycky et al. 2014). It is particularly interesting to study the few remaining resonant chains because it can help us to understand the early life of planetary systems. K2-19 (Foreman-Mackey et al. 2015; Montet et al. 2015; Armstrong et al. 2015) is one of these systems. It is composed of three known transiting planets: an inner Earth-size planet (K2-19 d, 2.5 days period, Vanderburg et al. 2016), and an outer pair of Neptunian planets (K2-19 b and c) inside the 3:2 MMR (with periods 7.9 and 11.9 days) that present significant transit-timing variations (TTVs; Agol et al. 2005; Holman & Murray 2005). These TTVs allowed the first measurements of the masses of K2-19 b and c (Barros et al. 2015; Narita et al. 2015). The latest characterization of the system by Petigura et al. (2020), who used a mix of TTVs and a photodynamical modeling (Carter et al. 2011), found eccentricities of  $0.20 \pm 0.03$  and  $0.21 \pm 0.03$  for K2-19 b and c, respectively. Disk migration does not favor significant orbital eccentricity excitation, however, because planet-disk interactions tend to damp eccentricities (Bitsch et al. 2013). Petit et al. (2020) proposed secular angular momentum exchange with the interior

planet d at 2.5 days, as well as an additional planet in the system. When this additional planet is included, the eccentricities of K2-19 b and c are reduced.

The precision of the radial velocities in the K2-19 system is moderate because the target is faint, and significant variability is caused by stellar activity (Dai et al. 2016; Nespral et al. 2017; Petigura et al. 2020). Therefore, transit photometry (notably through TTVs) remains the main technique for investigating this system, and it alone currently has the sensitivity to accurately measure orbital eccentricities and mutual inclinations. These measurements might help us to unveil the formation history of the system.

Motivated by the work of Petit et al. (2020), we obtained additional transit observations of K2-19 b and c with several facilities from the ground and space. They extend the observing baseline of Petigura et al. (2020) from 3 to 10 years and cover more than a complete superperiod (Lithwick et al. 2012). With 18 and 9 additional transits of planets b and c, respectively, we find that the system is considerably closer to the stationary state of the 3:2 resonance (see Fig. 8). Our posterior included non-aligned systems with very little free eccentricity (consistent with the standard model of disk migration) as well as aligned systems with a free eccentricity no higher than 0.1. The forced eccentricities of planets b and c are about 0.015 and 0.045 for all samples in the posterior (see Sect. 5.3).

The article is organized as follows: We present the new transit photometry of K2-19 b and c in Sect. 2. We revise the stellar parameters in Sect. 3. We describe our analysis in Sect. 4, and

\* This study uses CHEOPS data observed as part of the guest observer programmes PR240003 (PI Jiang) and PR240013 (PI Almenara).

we present our results in Sect. 5. Finally, we discuss our results in Sect. 6.

## 2. Observations

Table 1 summarizes all transit observations we used. We detail the new observations by telescope below together with the revision of two datasets from the literature.

### 2.1. K2

K2-19 was discovered during Campaign 1 of the K2 mission of the *Kepler* space telescope (Borucki et al. 2010). The light curve presents significant systematics because the fine-pointing capability of the spacecraft was lost. We used EVEREST (Luger et al. 2016, 2018) to correct for these systematics by masking the transits of the known transiting planets (including candidate K2-19 e; Sect. 4.1) to minimize changes in the transits during the detrending process.

### 2.2. LCOGT

Petigura et al. (2020) presented one partial transit of K2-19 b observed with the Las Cumbres Observatory Global Telescope (LCOGT; Brown et al. 2013) on June 25, 2017<sup>1</sup>, using a 1 m telescope at the South African Astronomical Observatory. We reanalyzed these transit data because we found that the transit timing reported by Petigura et al. (2020) deviated from the model posterior (Sect. 4.2) by  $3.5\sigma$  (equivalent to  $12.4 \pm 3.6$  minutes<sup>2</sup>). We note that the observations they interpreted as the transit ingress were acquired during twilight. We performed photometry with prose (Garcia et al. 2022) on images calibrated with the standard LCOGT pipeline (BANZAI; McCully et al. 2018).

### 2.3. ExTrA

We started our follow-up of K2-19 b and c in 2021 with the facility called Exoplanets in Transits and their Atmospheres (ExTrA; Bonfils et al. 2015), which is located at La Silla Observatory in Chile. ExTrA is a low-resolution near-infrared (0.85 to 1.55  $\mu$ m) multi-object spectrograph fed by three 60 cm telescopes. We used 8'' aperture fibers and the lowest-resolution mode ( $R \sim 20$ ) of the spectrograph with an exposure time of 60 seconds. During the 2021 and 2022 seasons, we targeted several transit windows of K2-19 b and c using the transit forecast from Petigura et al. (2020), which had uncertainties between 35 and 65 minutes for K2-19 b and between 2 and 4 hours for K2-19 c. We were able to observe one full transit and two partial transits of K2-19 b and no transit of K2-19 c. The observed transits of K2-19 b differed between  $2.5\sigma$  to  $4.5\sigma$  from the predictions by Petigura et al. (2020). From season 2023 onward, we used a TTV modeling of the available timings to forecast transits for ExTrA and other facilities. As K2-19 b and c have detected gravitational interactions, the observations of K2-19 b also improved the transit forecast of K2-19 c. This allowed us to finally observe a transit of K2-19 c on April 19, 2023 with ExTrA, which to our knowledge is the first time that the transit of this 6-hour TTV planet has been observed from the ground.

### 2.4. TESS

The Transiting Exoplanet Survey Satellite (TESS; Ricker et al. 2015) observed K2-19 in sectors 45, 46, and 72 with a cadence of 2 minutes. For the analysis, we used the presearch data-conditioning simple aperture photometry (PDCSAP; Smith et al. 2012; Stumpe et al. 2012, 2014) light curve of K2-19 that was produced by the TESS Science Processing Operations Center (SPOC; Jenkins et al. 2016).

### 2.5. CHEOPS

The CHaracterising ExOPlanet Satellite (CHEOPS; Benz et al. 2021) observed two transits of K2-19 b on February 29, 2024 and May 10, 2024, and one transit of K2-19 c on March 29, 2024 (Table 2). The raw data were automatically processed by the CHEOPS data reduction pipeline (DRP, version 14.1.3; Hoyer et al. 2020). We performed point-spread function photometry with the PIPE package<sup>3</sup> (Brandeker et al. 2024). Unfortunately, even with an observation efficiency of 93.7%<sup>4</sup>, no first contact of the transit of K2-19 c was observed.

### 2.6. EulerCam

We observed two transits of K2-19 b on March 8 and 16, 2024, and one transit of K2-19 c on May 4, 2024 with the Euler-Cam (ECAM) at the Swiss 1.2 m Euler telescope located at La Silla Observatory. The image reduction was carried out following Lendl et al. (2012) and Lendl (2014). Aperture photometry was performed using prose (Garcia et al. 2022), which relies on astropy (Astropy Collaboration et al. 2013, 2018, 2022) and photutils (Bradley 2023). The optimal differential photometry followed Broeg et al. (2005).

## 3. Stellar parameters

To determine the stellar parameters of K2-19, we fit its spectral energy distribution (SED) using stellar atmosphere and evolution models, along with the parallax determination from Gaia (Gaia Collaboration et al. 2016, 2023). We constructed the SED of K2-19 using the magnitudes from Gaia data release 3 (Riello et al. 2021), the 2-Micron All-Sky Survey (2MASS; Skrutskie et al. 2006; Cutri et al. 2003), and the Wide-field Infrared Survey Explorer (WISE; Wright et al. 2010; Cutri et al. 2021). The measurements are listed in Table 3. We used the PHOENIX/BT-Settl (Allard et al. 2012) stellar atmosphere model and the two stellar evolution models Dartmouth (Dotter et al. 2008) and PARSEC (Chen et al. 2014). We modeled the SED using the procedure described by Díaz et al. (2014), with informative priors for the effective temperature ( $T_{\text{eff}}$ ), surface gravity ( $\log g$ ), and metallicity ( $[\text{Fe}/\text{H}]_*$ ) from Sousa et al. (2021), and for the distance from the Gaia zeropoint-corrected parallax (Lindegren et al. 2021). We added an uncertainty of 2% quadratically to the  $T_{\text{eff}}$  following Tayar et al. (2022). We used uninformative priors for the remaining parameters. We used a jitter (Gregory 2005) for each set of photometric bands (Gaia, 2MASS, and WISE). The offset in the posterior median between the two tested stellar evolution models is  $0.008 R_\odot$  and  $0.017 M_\odot$ . We merged the results from the two different stellar evolution models assuming an equal probability for each. The parameters priors and posteriors are listed

<sup>1</sup> The date for this transit reported in Sect. 2.3 of Petigura et al. (2020) do not correspond with the quoted timing in their Table 1.

<sup>2</sup> This offset suggests that the LCOGT model of Petigura et al. (2020) underestimates the transit duration by approximately 25 minutes.

<sup>3</sup> <https://github.com/alphapsa/PIPE>

<sup>4</sup> Efficiency refers to the proportion of the observational time during which usable data are acquired.

**Table 1.** Log of the transit observations of K2-19 b and c.

Epoch b	Epoch c	Mid-transit date (UT) YYYY-MM-DD	Telescope Instrument	Band	Exposure time (s)	Coverage	Data	Source
0 to 9	0 to 6	2014-06-04 to 2014-08-19	K2	Kepler	1765	Full	lc	This work
30		2015-01-28	FLWO 1.2 m	i'	30	Partial	tt	Narita et al. (2015)
34		2015-03-01	TRAPPIST-South	Exo	10	Full	tt	Narita et al. (2015)
34		2015-03-01	NITES	no filter	20	Partial	lc	Armstrong et al. (2015)
35		2015-03-09	1-m C2PU Omicron	Johnson-R	60	Full	lc	Barros et al. (2015)
36		2015-03-17	Belesta 82-cm	Johnson-R	120	Full	lc	Barros et al. (2015)
41		2015-04-25	OAO 1.88 m / MuSCAT	g', r', z <sub>s</sub>	60, 30, 60	Partial	tt	Narita et al. (2015)
133		2017-04-23	Spitzer	4.5 μm	2	Full	tt	Petigura et al. (2020)
	87	2017-04-08	Spitzer	4.5 μm	2	Full	tt	Petigura et al. (2020)
141		2017-06-25	LCOGT-SAAO 1 m	i'	120	Partial	lc	This work
150		2017-09-05	Spitzer	4.5 μm	2	Full	tt	Petigura et al. (2020)
	102	2017-10-04	Spitzer	4.5 μm	2	Full	tt	Petigura et al. (2020)
311		2021-03-03	ExTrA T23	ExTrA	60	Full	lc	This work
343, 345	228, 229	2021-11-11 to 2021-11-27	TESS s45	TESS	120	Full	lc	This work
346 to 349	230, 232	2021-12-05 to 2021-12-29	TESS s46	TESS	120	Full	lc	This work
361		2022-04-03	ExTrA T23	ExTrA	60	Partial	lc	This work
362		2022-04-11	ExTrA T23	ExTrA	60	Partial	lc	This work
398		2023-01-21	ExTrA T23	ExTrA	60	Partial	lc	This work
399		2023-01-29	ExTrA T123	ExTrA	60	Full	lc	This work
400		2023-02-06	ExTrA T123	ExTrA	60	Partial	lc	This work
	272	2023-04-19	ExTrA T23	ExTrA	60	Full	lc	This work
436, 438	290, 291	2023-11-18 to 2023-12-04	TESS s72	TESS	120	Full	lc	This work
449		2024-02-29	CHEOPS	CHEOPS	60	Intermittent	lc	This work
449		2024-02-29	ExTrA T12	ExTrA	60	Full	lc	This work
450		2024-03-08	Euler / ECAM	NGTS	60	Full	lc	This work
450		2024-03-08	ExTrA T12	ExTrA	60	Full	lc	This work
451		2024-03-16	Euler / ECAM	NGTS	[30, 35]	Full	lc	This work
451		2024-03-16	ExTrA T12	ExTrA	60	Partial	lc	This work
	301	2024-03-29	CHEOPS	CHEOPS	60	Intermittent	lc	This work
304		2024-05-04	Euler / ECAM	NGTS	75	Full	lc	This work
304		2024-05-04	ExTrA T23	ExTrA	60	Full	lc	This work
458		2024-05-10	CHEOPS	CHEOPS	60	Intermittent	lc	This work

**Notes.** The epoch is the number of orbital periods since the first observed transit. For the TESS observations, the sector number is specified after the s. For the ExTrA observations, T stands for telescope, and the numbers following it represent the specific telescopes that observed the transit. For example, T123 means that telescopes 1, 2, and 3 all observed the transit. The Data column indicates how each transit was incorporated into the analysis of Sect. 4.2. The term lc is used when the transit light curve was used, and tt is employed when only the transit timing determined in the literature was used.

**Table 2.** Log of CHEOPS observations.

File key	OBS ID	UTC start	Visit duration	Exposure time	Efficiency
CH_PR240003_TG000101_V0300	2361633	2024-02-29T02:44:43	47002 s	1 x 60.0 s	66.9%
CH_PR240013_TG000101_V0300	2377170	2024-03-29T01:48:43	41059 s	1 x 60.0 s	93.7%
CH_PR240003_TG000102_V0300	2410093	2024-05-10T07:38:43	47002 s	1 x 60.0 s	54.9%

in Table A.1. The data with the maximum a posteriori (MAP) stellar atmosphere model are shown in Fig. A.1. For the stellar radius, we used a systematic uncertainty floor of 4% following Tayar et al. (2022) (we added an uncertainty of 4% quadratically to the radius estimated with the SED analysis). We confirmed the mass values with the four stellar evolution models implemented by `kiauhoku` (Claytor et al. 2020) and determined a mean value of  $0.882 M_{\odot}$ , a standard deviation between models of  $0.012 M_{\odot}$ , and a maximum offset of  $0.026 M_{\odot}$ . Our mass value and uncertainty already encompass the differences between the models in `kiauhoku`. We compare the stellar parameters derived in this section (Table 3) with literature values listed in Table A.2. The stellar mass and radius were used as priors in the photodynamical modeling (Sect. 4.2).

We used the stellar mass and the stellar rotation period determined in Sect. 4.2 ( $P_{\text{rot}} = 18.36 \pm 0.51$  days) to derive a gyrochronological age, neglecting the influence of the planets. Based on the formulation of Barnes (2010) and Barnes & Kim (2010) with initial periods  $P_0$  between 0.12 and 3.4 days, the age is  $1.70 \pm 0.25$  Gyr (we added a 10% systematic error to the statistical error based on Meibom et al. 2015).

## 4. Analysis

### 4.1. Search for additional transiting planets

The K2 light curve of K2-19 is dominated by rotational modulation, with an amplitude variability (peak to peak) of about 1.2% and a periodicity of  $18.36 \pm 0.51$  days (Sect. 4.2). We searched for additional transiting planets in the K2 data using `nuance` (Garcia et al. 2024), a transit search algorithm that accounts for correlated noise (stellar variability in this case), which we modeled with the rotation kernel Gaussian process (GP).

We found the already known planets with an S/N of 54 (K2-19 b), 33 (K2-19 c), and 13 (K2-19 d). Then, we detected an additional signal, the candidate planet e, at 19.97 days with an S/N of 7.1 (Fig. 1). We fit this planet candidate with `juliet` (Espinoza et al. 2019; Speagle 2020) using `batman` (Kreidberg 2015) for the transit model and the quasi-periodic kernel GP included in `celerite` (Foreman-Mackey et al. 2017) to model the stellar variability. We modeled the K2 light curve without the transits of K2-19 b, c, and d. We used a normal prior for the stellar density and uninformative priors for the rest of the parameters. We obtained an orbital period of  $19.9657^{+0.0047}_{-0.0067}$  days,

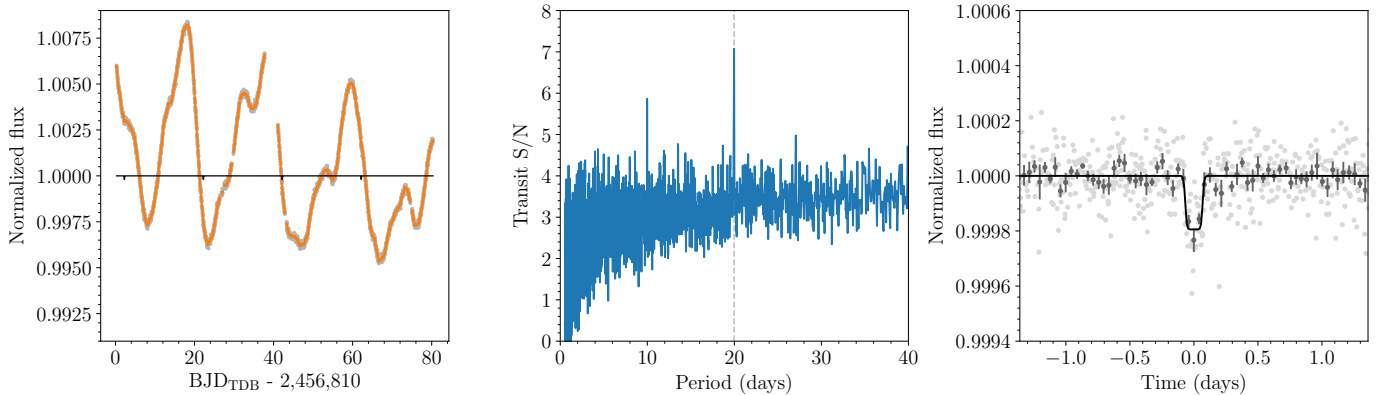


**Fig. 1.** Detection of the candidate planet e. *Left:* Gray data points represent the K2 data without the transits of planets b, c, and d. The orange data points show the mean GP model. The black light curve indicates the four transits we found. *Center:* Periodogram of the nuance algorithm. *Right:* Phased light curve without the noise model (gray points), binned (dark gray), and transit model (black line).

**Table 3.** Stellar parameters for K2-19 (EPIC 201505350, TIC 281885301, TOI-5145, Gaia DR3 3798833775141351552, and 2MASS J11395048+0036129).

Parameter	Value	Refs
<i>Astrometry</i>		
Right ascension (J2016), $\alpha$	11 <sup>h</sup> 39 <sup>m</sup> 50.46 <sup>s</sup>	1
Declination (J2016), $\delta$	00°36'12.95"	1
Parallax, $\pi$ (mas)	3.368 ± 0.020	1, 2
Distance, $d$ (pc)	296.9 ± 1.7	3
Proper motion $\alpha$ (mas/year)	-18.673 ± 0.022	1
Proper motion $\delta$ (mas/year)	4.571 ± 0.015	1
<i>Photometry</i>		
Kepler magnitude (mag)	12.806	4
TESS magnitude (mag)	12.3049 ± 0.0068	5
Gaia-BP (mag)	13.2080 ± 0.0030	1
Gaia-G (mag)	12.8060 ± 0.0028	1
Gaia-RP (mag)	12.2387 ± 0.0029	1
2MASS J (mag)	11.596 ± 0.024	6
2MASS H (mag)	11.208 ± 0.022	6
2MASS K <sub>s</sub> (mag)	11.161 ± 0.026	6
WISE W1 (mag)	11.105 ± 0.023	7
WISE W2 (mag)	11.152 ± 0.021	7
WISE W3 (mag)	10.92 ± 0.12	7
<i>Stellar parameters</i>		
Spectral type	G9	8
Prior stellar mass, $m_*$ ( $M_\odot$ )	0.885 ± 0.034	3
Prior stellar radius, $R_*$ ( $R_\odot$ )	0.845 ± 0.039	3
Effective temperature, $T_{\text{eff}}$ (K)	5350 ± 110	9, 3
Surface gravity, log $g$ (cgs)	4.531 ± 0.044	$R_*, m_*$
Metallicity, [Fe/H] <sub>*</sub> (dex)	0.03 ± 0.02	9
Age (Gyr)	1.70 ± 0.25	3

References : 1) [Gaia Collaboration et al. \(2023\)](#), 2) [Lindegren et al. \(2021\)](#), 3) This work, 4) [Huber et al. \(2016\)](#), 5) [Stassun et al. \(2019\)](#), 6) [Cutri et al. \(2003\)](#), 7) [Cutri et al. \(2021\)](#), 8) [Pecaut & Mamajek \(2013\)](#), 9) [Sousa et al. \(2021\)](#).

a transit duration of  $4.28 \pm 0.31$  hours, and a planet size of  $1.26 \pm 0.17 R_E$ . We repeated the analysis after removing the transits of the candidate planet e from the model. A model comparison strongly favors ([Kass & Raftery 1995](#)) the model with planet e over the model without the planet (log-Bayes factor  $Z_{\text{planet e}}/Z_{\text{no planet e}}$  of  $5.60 \pm 0.37$ ). We repeated the analysis with `juliet` with the timing of each transit as a free parameter. The individual timings have a precision of about 20 minutes and are

compatible with a linear ephemeris. Interestingly, the candidate planet e is close to the 5:3 MMR with K2-19 c. We included this planet candidate (K2-19 e) in the analysis of the system.

Subsequent searches yielded low S/N candidates that are not favored by the model comparison. One interesting candidate that emerged is a  $0.591 \pm 0.025 R_E$  planet with a period of 1.89 days (close to the 4:3 MMR with K2-19 d), however. When this candidate was added to the analysis described in Sect. 4.2, its mass was  $0.089 \pm 0.035 M_E$ .

#### 4.2. Photodynamical modeling

We fit the observed photometry accounting for the gravitational interactions between the five bodies assumed in the system using a photodynamical model. Its positions and velocities in time were obtained through an n-body integration. The sky-projected positions were used to compute the light curve ([Mandel & Agol 2002](#)) with `batman` ([Kreidberg 2015](#)) using a quadratic limb-darkening law ([Manduca et al. 1977](#)), which we parameterized following [Kipping \(2013\)](#). To account for the integration time of 30 minutes of the K2 light curve, the model was oversampled by a factor of 30, and then binned back to match the cadence of the data points ([Kipping 2010](#)). We used the n-body code `REBOUND` ([Rein & Liu 2012](#)) with the `WHFast` integrator ([Rein & Tamayo 2015](#)) and an integration step of 0.01 days, which resulted in a maximum error ([Almenara et al. 2018](#)) of  $\sim 5$  ppm for the photometric model. The light-time effect ([Irwin 1952](#)) was not included; with an expected amplitude of  $\sim 6$  ms in the transit timing, it is a negligible effect for this system. We included some transit timings from the literature, assuming that the reported time is the calculated time of minimum sky-projected planet-star separation. Table 1 specifies whether we used the time-series photometry or only the reported timing for each observation. The model was parameterized using the stellar mass and radius, limb-darkening coefficients, planet-to-star mass and radius ratios, and Jacobi orbital elements (Table 4) at the reference time,  $t_{\text{ref}} = 2456829.222$  BJD<sub>TDB</sub>, during the K2 observations. Because the problem is symmetrical, we fixed the longitude of the ascending node of K2-19 b  $\Omega_b$  at  $t_{\text{ref}}$  to  $180^\circ$ , and we limited the inclination of K2-19 c to  $i_c < 90^\circ$ . In order to reduce the correlation between the jump parameters, we used the [Huber et al. \(2013\)](#) parameterization for the eccentricity and the argument of pericenter of K2-19 b and c.

**Table 4.** Inferred system parameters.

Parameter	Units	Prior	Median and 68.3% CI	Prior	Median and 68.3% CI
<b>Star</b>					
Stellar mass, $m_\star$	( $M_\odot$ )	$N(0.885, 0.034)$	$0.892 \pm 0.034$		
Stellar radius, $R_\star$	( $R_\odot^N$ )	$N(0.845, 0.039)$	$0.824 \pm 0.024$		
Stellar mean density, $\rho_\star$	(g cm $^{-3}$ )		$1.59 \pm 0.12$		
Surface gravity, $\log g$	(cgs)		$4.556 \pm 0.024$		
K2 GP $P_{\text{rot}}$	(d)	$U(0.1, 100)$	$18.36 \pm 0.51$		
<b>Planets</b>					
Semi-major axis, $a$	(au)		<b>Planet b</b>	<b>Planet b</b>	<b>Planet c</b>
Eccentricity, $e$				$0.043 \pm 0.024$	$0.0982 \pm 0.0012$
Argument of pericenter, $\omega$	( $^\circ$ )			$197 \pm 26$	$252^{+18}_{-11}$
Inclination, $i$	( $^\circ$ )	$S(0, 180)$		$89.37 \pm 0.26$	$89.37 \pm 0.15$
Longitude of the ascending node, $\Omega$	( $^\circ$ )			$180$ (fixed at $t_{\text{ref}}$ )	$U(90, 270)$
Mean anomaly, $M_0$	( $^\circ$ )			$257 \pm 26$	$180.84 \pm 0.45$
Mass ratio, $m_p/m_\star$		$U(0, 1)$	$(10.357 \pm 0.085) \times 10^{-5}$	$U(0, 1)$	$(3.746 \pm 0.056) \times 10^{-5}$
Radius ratio, $R_p/R_\star$		$U(0, 1)$	$0.07332 \pm 0.00054$	$U(0, 1)$	$0.04321 \pm 0.00044$
Scaled semi-major axis, $a/R_\star$				$19.53 \pm 0.51$	$25.61 \pm 0.66$
Impact parameter, $b$				$0.217 \pm 0.089$	$0.299 \pm 0.065$
$T'_0 - 2\,450\,000$	(BJD <sub>TDB</sub> )	$U(5829, 7829)$	$6829.22231 \pm 0.00016$	$U(5829, 7829)$	$6829.18490 \pm 0.00054$
$P'$	(d)	$U(5, 10)$	$7.922806 \pm 0.000090$	$U(10, 15)$	$11.89770 \pm 0.00046$
$K'$	(m s $^{-1}$ )			$10.66 \pm 0.17$	$3.368 \pm 0.063$
Planet mass, $m_p$	( $M_E$ )			$30.8 \pm 1.3$	$11.12 \pm 0.44$
Planet radius, $R_p$	( $R_{eE}^N$ )			$6.59 \pm 0.22$	$3.88 \pm 0.14$
Planet mean density, $\rho_p$	(g cm $^{-3}$ )			$0.590 \pm 0.053$	$1.046 \pm 0.097$
Planet surface gravity, $\log g_p$	(cgs)			$2.841 \pm 0.028$	$2.859 \pm 0.028$
Equilibrium temperature, $T_{\text{eq}}$	(K)			$857 \pm 21$	$749 \pm 19$
Mutual inclination, $I_{b,c}$	( $^\circ$ )			$0.85 \pm 0.44$	
$e_c \cos \omega_c - \frac{a_b}{a_c} e_b \cos \omega_b$		$U(-1, 1)$	$0.00918 \pm 0.00020$		
$e_c \cos \omega_c + \frac{a_b}{a_c} e_b \cos \omega_b$		$U(-1, 1)$	$-0.050 \pm 0.040$		
$e_c \sin \omega_c - \frac{a_b}{a_c} e_b \sin \omega_b$		$U(-1, 1)$	$-0.05386 \pm 0.00082$		
$e_c \sin \omega_c + \frac{a_b}{a_c} e_b \sin \omega_b$		$U(-1, 1)$	$-0.071 \pm 0.027$		
<b>Planets</b>					
Semi-major axis, $a$	(au)		<b>Planet d</b>	<b>Planet d</b>	<b>Candidate planet e</b>
Eccentricity, $e$				$0.03478 \pm 0.00043$	$0.1387 \pm 0.0017$
Argument of pericenter, $\omega$	( $^\circ$ )			$< 0.44^\dagger$	$< 0.15^\dagger$
Inclination, $i$	( $^\circ$ )	$S(0, 180)$		$248^{+72}_{-110}$	$245 \pm 37$
Longitude of the ascending node, $\Omega$	( $^\circ$ )	$U(90, 270)$		$89.7 \pm 1.6$	$S(0, 180)$
Mean anomaly, $M_0$	( $^\circ$ )			$179.3 \pm 7.3$	$U(90, 270)$
$\sqrt{e} \cos \omega$		$U(-1, 1)$		$200 \pm 100$	
$\sqrt{e} \sin \omega$		$U(-1, 1)$		$0.02 \pm 0.27$	$U(-1, 1)$
Mass ratio, $m_p/m_\star$		$U(0, 1)$		$-0.17^{+0.22}_{-0.15}$	$-0.174 \pm 0.068$
Radius ratio, $R_p/R_\star$		$U(0, 1)$		$< 2.1 \times 10^{-5}^\dagger$	$< 0.67 \times 10^{-5}^\dagger$
Scaled semi-major axis, $a/R_\star$				$U(0, 1)$	$0.0135 \pm 0.0016$
Impact parameter, $b$				$9.07 \pm 0.24$	$36.17 \pm 0.94$
$T'_0 - 2\,450\,000$	(BJD <sub>TDB</sub> )	$U(5829, 7829)$		$0.17^{+0.18}_{-0.12}$	$0.544^{+0.099}_{-0.15}$
$P'$	(d)	$U(0, 5)$		$6828.9909 \pm 0.0035$	$U(5829, 7829)$
$K'$	(m s $^{-1}$ )			$2.50827^{+0.00027}_{-0.00014}$	$19.9724 \pm 0.0054$
Planet mass, $m_p$	( $M_E$ )			$< 3.1^\dagger$	$< 0.51^\dagger$
Planet radius, $R_p$	( $R_{eE}^N$ )			$< 6.2^\dagger$	$< 2.0^\dagger$
Planet mean density, $\rho_p$	(g cm $^{-3}$ )			$1.044 \pm 0.064$	$1.22 \pm 0.15$
Planet surface gravity, $\log g_p$	(cgs)			$< 31^\dagger$	$< 8.4^\dagger$
Equilibrium temperature, $T_{\text{eq}}$	(K)			$2.95 \pm 0.63$	$2.46 \pm 0.40$
				$1258 \pm 31$	$630 \pm 16$

**Notes.** The table lists the prior, the posterior median, and the 68.3% CI for the photodynamical analysis (Sect. 4.2). The Jacobi orbital elements are given for the reference time  $t_{\text{ref}} = 2\,456\,829.222$  BJD<sub>TDB</sub>.  $^\dagger$  Upper limit at 99% confidence. The planetary equilibrium temperature is computed for zero albedo and full day-night heat redistribution.  $P'$  and  $T'_0$  should not be confused with the period or the time of conjunction, respectively, and they were only used to reduce the correlations between jump parameters, replacing the semimajor axis and the mean anomaly at  $t_{\text{ref}}$ .  $T'_0 \equiv t_{\text{ref}} - \frac{P'}{2\pi} (M_0 - E + e \sin E)$  with  $E = 2 \arctan \left\{ \sqrt{\frac{1-e}{1+e}} \tan \left[ \frac{1}{2} (\frac{\pi}{2} - \omega) \right] \right\}$ .  $P' \equiv \sqrt{\frac{4\pi^2 a^3}{Gm_\star}}, K' \equiv \frac{m_p \sin i}{m_\star^{2/3} \sqrt{1-e^2}} \left( \frac{2\pi G}{P'} \right)^{1/3}$ . CODATA 2018:  $G = 6.674\,30 \times 10^{-11}$  m $^3$  kg $^{-1}$  s $^{-2}$ . IAU 2012: au = 149 597 870 700 m. IAU 2015:  $R_\odot^N = 6.957 \times 10^8$  m,  $(GM)_\odot^N = 1.327\,124\,4 \times 10^{20}$  m $^3$  s $^{-2}$ ,  $R_{eE}^N = 6.378\,1 \times 10^6$  m,  $(GM)_E^N = 3.986\,004 \times 10^{14}$  m $^3$  s $^{-2}$ ,  $M_\odot = (GM)_\odot^N/G$ ,  $M_E = (GM)_E^N/G$ ,  $k^2 = (GM)_\odot^N/(86\,400\,000)^2/\text{au}^3$ .  $N(\mu, \sigma)$ : Normal distribution with mean  $\mu$  and standard deviation  $\sigma$ .  $U(a, b)$ : A uniform distribution defined between a lower  $a$  and upper  $b$  limit.  $S(a, b)$ : A sinusoidal distribution defined between a lower  $a$  and upper  $b$  limit. Transits occur when the sum of the true anomaly and the argument of pericenter equals  $-90^\circ$ .

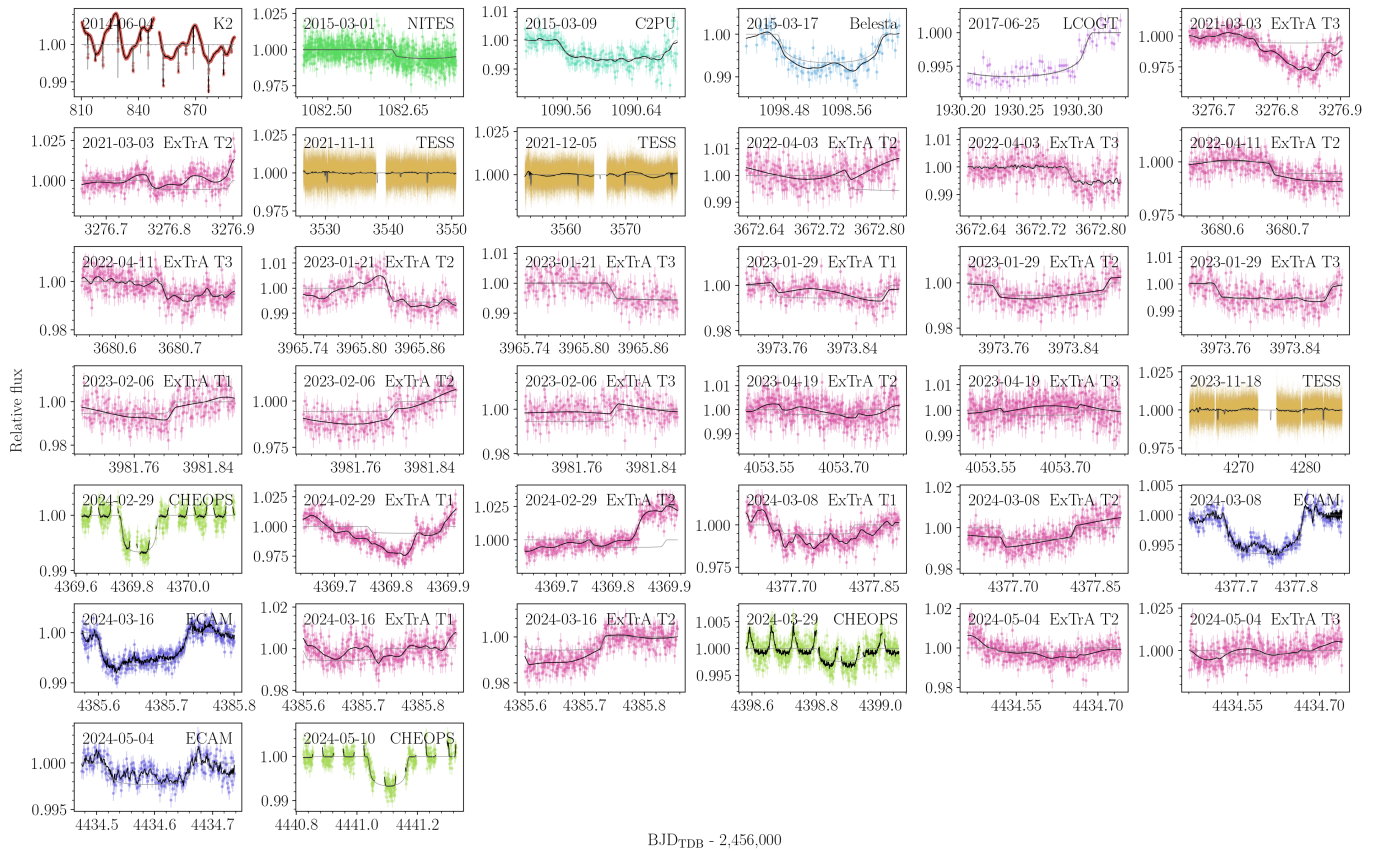


**Fig. 2.** Photodynamical modeling of the transit photometry. Each dataset is shown in a different panel, labeled with the midtransit date (or the start date of the observation for K2 and TESS) and the telescope (or instrument). The error bars, in different colors for each telescope, represent the observations. The black line shows the MAP model that combines transits and noise. The gray line shows the transit model.

We used a GP regression (`celerite`; Foreman-Mackey et al. 2017) for the model of the error terms of the transit light curves. We used the rotational kernel for K2 and an approximate Matern kernel for the rest of the datasets. For CHEOPS observations, we used the satellite roll angle as a regressor instead of the time for the rest, and we added a linear model with log-background (for the transit on May 10, 2024, we also added a quadratic term). For the ECAM transits, we added linear models with the point spread function centroid shifts, full width at half maximum, and peak flux value, and a quadratic term for the airmass.

In total, the model had 149 free parameters. We used normal priors for the stellar mass and radius from Sect. 3 and uninformative prior distributions for the rest of the parameters. The joint posterior distribution was sampled using the `emcee` algorithm (Goodman & Weare 2010; Foreman-Mackey et al. 2013).

Our parameterization of the eccentricity and argument of pericenter for planets b and c leads to a nonuniform prior in eccentricity. To account for this, we applied the algorithm called sampling importance resampling (SIR; Rubin 1987) as an a posteriori correction.

## 5. Results

In Table 4 we list the median and the 68% credible interval (CI) of the marginal distribution of the inferred system parameters. The one- and two-dimensional projections of the posterior sample of selected system parameters are shown in Fig. A.2. The MAP model of the transit photometry is plotted in Fig. 2. The noise-model-corrected transits for each planet are plotted in Figs. A.3 to A.6. Figure A.7 shows the posterior of the planet

orbits. The value of  $P_{\text{rot}}$  derived from the K2 data with the `celerite` rotational kernel is  $18.36 \pm 0.51$  days, which is lower ( $3.7\sigma$ ) than the  $20.54 \pm 0.30$  days of (Nespral et al. 2017) that were obtained by applying the autocorrelation function (McQuillan et al. 2013) to the K2 light curve.

The current transit-timing  $1\sigma$  uncertainty for K2-19 d and e is about 7 and 33 hours, respectively. With a transit depth of about 190 and 270 ppm for K2-19 d and e, respectively, these planets are difficult to follow-up (or confirm). Notably, their shallow transit depths place them below the detection threshold of TESS, which otherwise would have been well suited for recovering planets with currently poorly constrained ephemerides. In addition, K2-19 e might not always transit in the long term (Sect. 5.2). If the candidate K2-19 e is not real, the data provide an upper limit of  $2.0 M_E$  at a confidence of 99% for a body in 5:3 MMR with K2-19 c. We verified the results for planets b and c did not change significantly when planet e was excluded from the model. In the subsequent sections, we concentrate on K2-19 b and c because we have achieved a more detailed characterization of these planets.

### 5.1. Evolution of the orbital parameters during the observations

We studied the changes in the orbital parameters of the planets during the period covered by the observations (10 years) from 1000 random draws from the posterior distribution. The eccentricities of K2-19 b and c vary significantly during the observations for most posterior samples and are correlated. The peri-

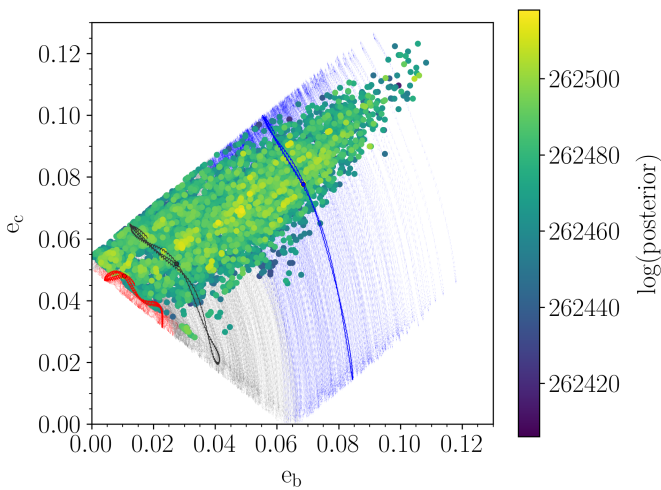


**Fig. 3.** Correlation of the eccentricities of K2-19 b and K2-19 c. The dots represent the posterior samples at  $t_{\text{ref}}$ , and the color scale shows their log-posterior value. The evolution during the observations for 1000 random draws from the posterior distribution is shown in light gray (black for a random sample), light red (red for a random sample), and light blue (blue for the MAP model). The color coding depends on whether  $\varpi_b - \varpi_c$  circulates, librates around  $\pi$ , or librates around zero (the same scheme as in Fig. 4). The blue dot represents the MAP model values at  $t_{\text{ref}}$  (and from there, it starts to move upward), and similarly for the two random samples in red (left) and black (upward). Section 5.4 discusses the shape of the domain and resonance angle behavior.

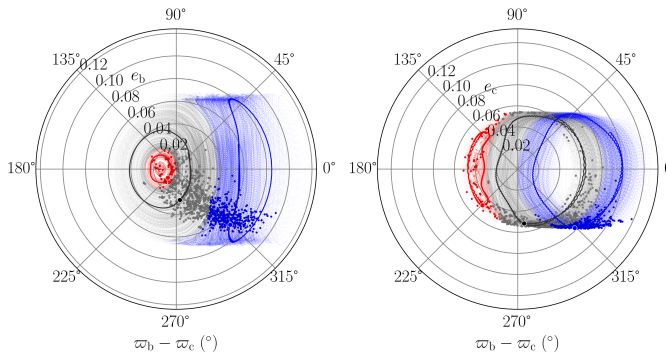


**Fig. 4.** Correlation of the eccentricity of K2-19 b (left panel) and K2-19 c (right panel) with the difference in the longitudes of periastron over the time span covered by the observations for 1000 random draws from the posterior distribution. Samples that circulate are shown in light gray (one random sample is shown in black), those that librate around  $\varpi_b - \varpi_c = 0^\circ$  are shown in light blue, and those that librate around  $\varpi_b - \varpi_c = 180^\circ$  are shown in light red (one random sample is shown in red). The MAP model, which librates around 0, is shown in blue. The dots, with the same color code, represent the positions at  $t_{\text{ref}}$ .

odicity is generally dominated by the superperiod (Fig. 3). The correlation between the eccentricities and difference in the longitudes of periastron exhibits three types of behavior (see Fig. 4): Libration around  $\varpi_b - \varpi_c = 0^\circ$  (53% of the posterior samples), circulation (41%), and libration around  $\varpi_b - \varpi_c = 180^\circ$  (6%). This behavior is discussed in detail in the companion paper (hereafter C2).

The period ratio librates around its mean value  $3/2 + \Delta\sigma$  with a small amplitude  $A_\sigma\Delta\sigma$  and with a period equal to the resonant period (see Sect. 5.3), each determined by conditions at the time of formation, which generally result in two-planet systems having period ratios slightly larger than exact commensurabil-

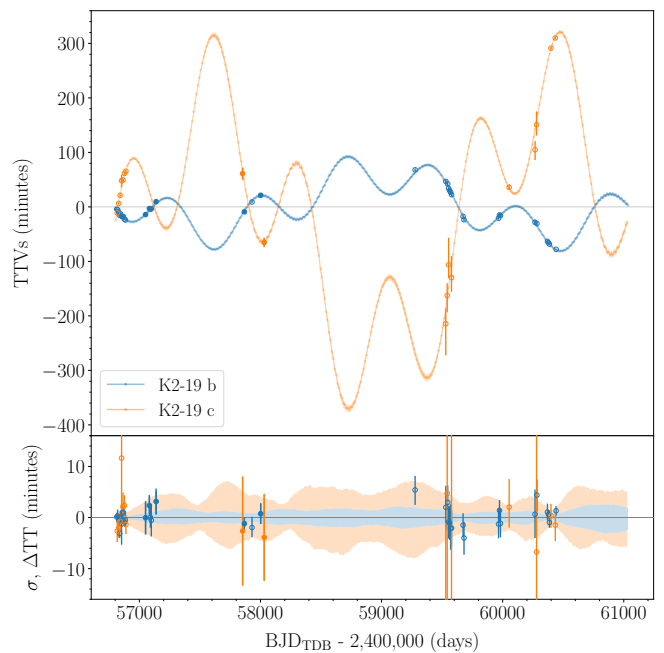


**Fig. 5.** Posterior TTV predictions of K2-19 b (blue band) and K2-19 c (orange band) computed relative to a linear ephemeris ( $2456813.386969 + 7.9209002 \times \text{epoch}$  [BJD<sub>TDB</sub>],  $2456817.280436 + 11.8983248 \times \text{epoch}$  [BJD<sub>TDB</sub>]) for planet b and c, respectively). We used 1000 random draws from the posterior distribution to estimate the TTV median value and its uncertainty (68.3% CI). In the upper panel, the posterior TTV values are shown and compared with individual transit-time determinations (Sect. B, open and filled error bars). The filled error bars were used as data in the modeling. In the lower panel, the posterior median transit-timing value was subtracted to visualize the uncertainty of the distribution. The posterior median transit time was also subtracted from each observed epoch for the individual transit-time determinations to allow a better comparison with the posterior of the photodynamical modeling.

ity (Fabrycky et al. 2014). The posterior median and 68.3% CI values for  $\Delta\sigma$  and  $A_\sigma$  are  $0.00291^{+0.00001}_{-0.00002}$  and  $0.40 \pm 0.02$ , respectively, suggesting that the system is resonant and close to its equilibrium state (Sect. 5.3).

## 5.2. Secular behavior

Over longer timescales, the precession of the orbital planes exhibits a period of approximately 165 years (Fig. A.10), which results in oscillations in both the difference in orbital inclinations and the relative longitudes of the ascending nodes. During certain epochs, this configuration permits mutual eclipses between planets b and c.

## 5.3. Transit-timing variations: Mass estimates

Figure 5 shows the posterior TTVs of K2-19 b and c, obtained from the times of minimum projected separation of the star and planet. Two well-separated periodicities are clearly evident, with the ratio of the associated super and (shorter, noncommensurate) resonant periods,  $P_S$  and  $P_R$ , respectively, which immediately indicates that the system is formally resonant and in the librating state, even before any analysis is performed. Moreover, the magnitudes of the amplitudes of each component are similar, which reveals (again without a detailed analysis) that the system is close to (but not at) the equilibrium state of the resonance

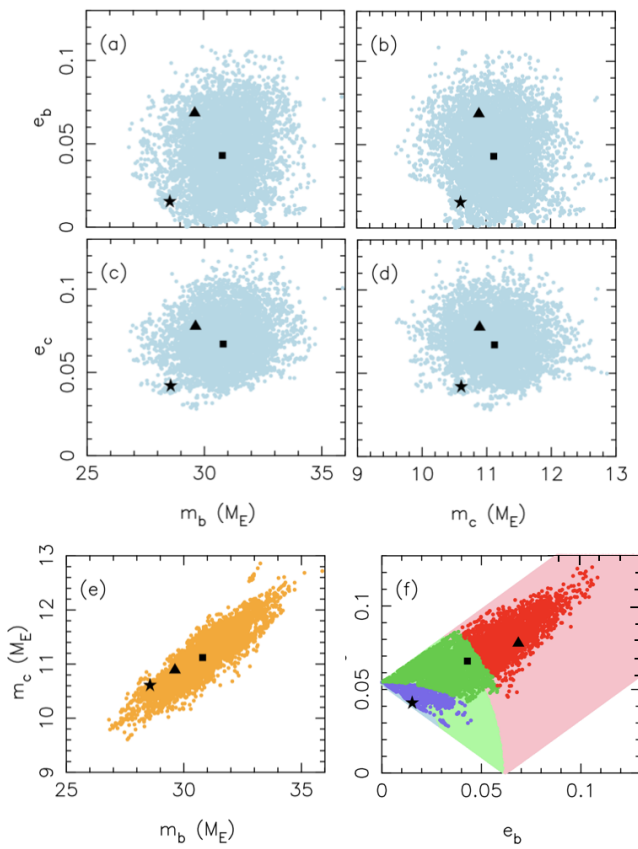


**Fig. 6.** Posterior projections of the mass and eccentricity distributions. They demonstrate that the eccentricities and planet masses are hardly correlated (panels a-d), while the planet masses themselves are correlated (panel e), as are the eccentricities (panel f). The color scheme in (f) is purple for when both resonance angles librate such that  $\varpi_b - \varpi_c \equiv \Delta\varpi$  librates around  $\pi$ ; green for when  $\phi_1$  circulates and  $\phi_2$  librates so that  $\Delta\varpi$  circulates; red for when both resonance angles circulate such that  $\Delta\varpi$  librates around zero; and pink and light green for the possible values of the eccentricities given the MAP value of  $u$  and arbitrary values of  $v$ . The true resonance angle  $\psi$  librates with a small amplitude around zero for all posterior solutions (Sect. 5.4 and Fig. 8). The stars indicate the posterior sample closest to the fixed-point eccentricities, and the squares and triangles indicate the median and MAP values, respectively. Fig. A.2 shows the projections of the other parameters.

(cyan star in Fig. 8): This is the primary fixed point of the phase space in which the system resides. An algorithm for drawing these conclusions by simple inspection is given in C2.

When a system is in this state and the quality of the timing data is high enough, the Bayesian analysis process is expected to find little correlation between the masses and eccentricities, in contrast to the mass-eccentricity degeneracy that is understood to plague many systems exhibiting TTVs. Figure 6 shows selected posterior projections (see also Figure A.2), demonstrating that this is indeed the case for the K2-19 system, while the planet masses themselves are correlated, as are the two eccentricities (panels (e) and (f), respectively). A full analysis of the nature of these correlations is presented in C2 (see also Nesvorný & Vokrouhlický 2016), but we note that the masses can be determined independently when the resonant and superfrequencies are distinct and their associated Fourier contributions to the TTV signal can be accurately separated and modeled. Moreover, while in general the interference between the resonant and super harmonics is nonlinear, for a system close to the primary

fixed point such as K2-19 b,c there is little interference, and the masses can be directly determined from the amplitudes of the supercomponent together with the ratio of the superperiod and resonant period. This result is summarized below, and a more general treatment for systems that are not necessarily close to the primary fixed point (using the information in the resonant harmonic) is presented in C2.

The analysis in C2 is based on a new formalism for the study of the dynamics of systems near first-order resonances (Mardling, in prep.). A key result we used here is that for a system that is close to the primary fixed point of the forced part of the associated phase space,<sup>5</sup> a quantity  $R$  called the *resonance parameter* relates the ratio of the superperiod to the resonant period to the planet-to-star mass ratios such that

$$\begin{aligned} R &= (P_S / P_R)^2 - 1 \\ &= 3 \left( \frac{\sigma}{\Delta\sigma} \right)^2 (\bar{m}_b + \alpha \bar{m}_c) (v_1(\alpha) e_b^{(+)} + v_2(\alpha) e_c^{(+)}) , \end{aligned} \quad (1)$$

for a system close to the  $n+1:n$  commensurability. Here,  $\sigma = (n+1)/n$ ,  $\alpha = \sigma^{-2/3}$  is the ratio of the semimajor axes at exact commensurability,  $\Delta\sigma$  is the distance of the primary fixed point to exact commensurability,<sup>6</sup>  $\bar{m}_{b,c} = m_{b,c}/m_*$  are the planet-to-star mass ratios,  $v_1(\alpha)$  and  $v_2(\alpha)$  are constants related to Laplace coefficients, such that  $v_1 = -2.025$  and  $v_2 = 2.484$  for  $\sigma = 3/2$ , and

$$e_b^{(+)} = \frac{\alpha^{-1/2} |v_1| \bar{m}_c}{n \Delta\sigma} \quad \text{and} \quad e_c^{(+)} = \frac{v_2 \bar{m}_b}{n \Delta\sigma} \quad (2)$$

are the values of the forced eccentricities at the primary fixed point. Equation (1) represents one constraint on the three quantities  $\bar{m}_b$ ,  $\bar{m}_c$ , and  $\Delta\sigma$ . The other two come from the amplitudes of the supercomponents of the TTV signals, as described below.

As discussed in C2, an accurate model for the TTVs of a system in the librating state is such that the  $j$ th TTV of planet b is given by

$$\begin{aligned} \text{TTV}_b(j) &= A_S^{(b)} \cos[v_S(t_j - t_{\text{ref}}) + \beta_S] \\ &\quad + A_R^{(b)} \cos[v_R(t_j - t_{\text{ref}}) + \beta_R] + c_1^{(b)} t_j + c_0^{(b)} \end{aligned} \quad (3)$$

with a similar expression for the  $k$ th TTV of planet c. Here,  $t_j$  is the  $j$ th midtransit time,  $t_{\text{ref}}$  is the reference time,  $\bar{P}_b$  is the long-term average value of the inner orbital period, which is well approximated by its linear ephemeris value for a long enough baseline,  $A_S^{(b)}$  and  $A_R^{(b)}$  are the amplitudes of the supercomponent and resonant component,  $\beta_S$  and  $\beta_R$  are the associated phases, and  $c_0^{(b)}$  and  $c_1^{(b)}$  are constants that tend to zero in the case of an unlimited observing baseline (or more generally, model any long-term secular trends that are not accounted for in the model). For our purposes, we have in particular that

$$A_S^{(b)} \simeq \bar{P}_b e_b^{(+)} / \pi \propto \bar{m}_c \quad \text{and} \quad A_S^{(c)} \simeq \bar{P}_c e_c^{(+)} / \pi \propto \bar{m}_b , \quad (4)$$

where  $e_b^{(+)}$  and  $e_c^{(+)}$  are given in (2), while  $A_R^{(b)} \propto \bar{m}_c$  and  $A_R^{(c)} \propto \bar{m}_b$  and the phases  $\beta_S$  and  $\beta_R$  depend on the forced eccentricities away from their fixed-point values (C2). If the K2-19 b,c system were precisely at the fixed point, we would have  $A_R^{(b)} = A_R^{(c)} = 0$  and

$$\beta_S = n\lambda_b(t_{\text{ref}}) - (n+1)\lambda_b(t_{\text{ref}}) , \quad (5)$$

<sup>5</sup> We refer to the forced and free eccentricity and defer their definitions to C2.

<sup>6</sup> Note that for a long enough baseline,  $\Delta\sigma \simeq \Delta S \equiv \bar{P}_c / \bar{P}_b - (n+1)/n$  for systems close to the fixed point.

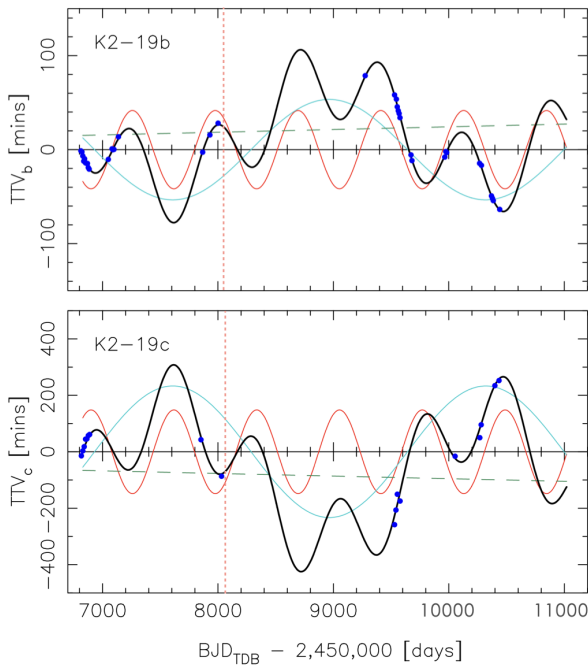


**Fig. 7.** Least-squares fits of the TTV data shown in Fig. 5 (blue dots). The red and cyan curves show the individual resonant and superharmonics, while the dashed green lines show the linear offsets. The black curves show the sum of all three, and the vertical dotted lines indicate the observing baseline of Petigura et al. (2020). The two panels use different y-axis scales.

the latter being minus the longitude of conjunctions at the reference time, while if the system were farther from the fixed point, the resonant contribution would dominate the TTV signal. Figure 7 plots the best fits to the median TTV values shown in Fig. 5, and the individual contributing harmonics and residual linear trends, verifying that the superamplitude and resonant amplitude are similar, while  $P_S/P_R \approx 3.8$ . The values for the Fourier parameters are listed in Table 5, together with  $R$ ,  $\Delta\sigma$ ,  $e_b^{(+)}$  and  $e_c^{(+)}$ . The planet mass estimates listed in the column labeled ‘‘Fourier’’ were obtained by solving (1), (2) and (4) for  $\bar{m}_b$ ,  $\bar{m}_c$  and  $\Delta\sigma$ , yielding values that are 2.5% and 0.4% lower than the median values obtained from the photodynamical analysis for planets b and c, respectively, and are well inside our error bars. We also list our median and MAP values for the planet masses (taken from Table 4) and those of Petigura et al. (2020).

The accuracy of the Fourier mass estimates can be attributed to a good estimate of  $\Delta\sigma$  via the resonance parameter  $R$  (which is vital because the superamplitudes go like  $m_{b,c}/\Delta\sigma$ ); if we had used  $\Delta S = \bar{P}_c/\bar{P}_b - (n+1)/n$  as an estimate for  $\Delta\sigma$  in (4), the planet masses would both have been underestimated by about 30%.

#### 5.4. Transit-timing variations: Eccentricity constraints

The high eccentricities of K2-19 b and c reported by Petigura et al. (2020) (both about 0.2) have inspired much discussion about the formation of the system, including the influence of additional planets (e.g., Petit et al. 2020; Laune et al. 2022; Choksi & Chiang 2023; Goldberg & Batygin 2023) and stochastic stirring by turbulent eddies (Goldberg & Batygin 2023). Based on seven additional years of transit data, however, our posterior is significantly better constrained, with median and 68.3% CI val-

ues at  $e_b = 0.043 \pm 0.024$  and  $e_c = 0.067 \pm 0.017$ . While substantially lower than 0.2, these values still imply some free eccentricity, with values lower than 0.005 unlikely at a confidence of 99%. Panel (f) of Figure 6 again shows the posterior coverage of the  $e_b - e_c$  plane (see the figure caption for the meaning of the colors and the discussion below). The shape of this posterior projection is a result of a third integral (in addition to the total energy and angular momentum), which exists at first order in eccentricity for systems that are close to a first-order commensurability. Because of this integral, the free components of the Runge-Lenz vectors for each planet orbit are approximately constant, and as a result, their contribution to the TTVs is limited because their variation in time is second order in eccentricity. This leads to the degeneracy that is visible in the figure and is confined to the upper half of the allowed region (the latter being the entire colored part) as a result of second-order effects and of the sensitivity to the average transit duration time (see the next section).

The colors in Figure 6(f) are associated with the libration and/or circulation behavior of the standard resonance angles  $\phi_1 = n\lambda_b - (n+1)\lambda_c + \varpi_b$  and  $\phi_2 = n\lambda_b - (n+1)\lambda_c + \varpi_c$  and the difference in the longitudes of periastron  $\varpi_b - \varpi_c$ ; this can be derived from the new definitions of forced and free eccentricity given in C2 together with the complex functions<sup>8</sup>

$$u = -3 \left( \frac{\sigma}{\Delta\sigma} \right)^2 (\bar{m}_b + \alpha \bar{m}_c) (v_1 z_b + v_2 z_c) \quad (6)$$

and

$$v = -3 \left( \frac{\sigma}{\Delta\sigma} \right)^2 (\bar{m}_b + \alpha \bar{m}_c) (g^{-1} v_2 z_b - g v_1 z_c), \quad (7)$$

posterior values that are plotted in Figure 8. Here,  $g = (m_c/m_b)^{1/2} \alpha^{-1/4}$ ,  $z_1 = e_b e^{i\phi_1}$  and  $z_2 = e_c e^{i\phi_2}$ . We note from (1) that  $u = R$  at the primary fixed point (at which  $\phi_1 = 0$  and  $\phi_2 = \pi$ ). We also note that the true resonance angle  $\psi$ , defined such that  $u = |u| e^{i\psi}$ , librates with a small amplitude for the whole posterior. Finally, we note that the third integral mentioned above is simply  $uv^* = \text{constant}$  (so that the radius of the black curve in the right panel of Figure 8 is constant). The details are provided in C2.

#### 5.5. The transit duration: Further eccentricity constraints

The transit duration was computed as the difference between the first and fourth contact using the sky-projected planet-star separation. The transit durations of K2-19 b and c are shown in Fig. 9 and exhibit transit duration variations (TDVs). The transit duration of K2-19 b varies by about 6 minutes peak to peak over the 10-year baseline, and that of K2-19 c varies by about 20 minutes. This is 3% and 11%, respectively, of the median transit durations. As we show in C2 the variation period is the super-period, and the amplitudes are proportional to the primary fixed-point eccentricities  $e_b^{(+)}$  and  $e_c^{(+)}$  and not the true eccentricities, as is commonly assumed. The average transit durations of planets b and c do provide constraints via the quantities  $e_b \sin \omega_b$  and  $e_c \sin \omega_c$ , however, which further confines the  $e_b - e_c$  posterior projection in the upper half of the colored region in panel (f) of Figure 6.

<sup>7</sup> The median and 68.3% CI values of their magnitudes are  $e_b^{(\text{free})} = 0.046 \pm 0.023$  and  $e_c^{(\text{free})} = 0.037 \pm 0.019$ , and are related via  $e_b^{(\text{free})}/e_c^{(\text{free})} = v_2/|v_1|$  (C2).

<sup>8</sup>  $u$  and  $v$  are the equivalent of  $Y_1$  and  $Y_2$  in Petit et al. (2020) with different scalings.

**Table 5.** Fourier and photodynamical mass estimates

Parameter	Units	Median and 68.3% CI Photodyn 10 yr	MAP Photodyn 10 yr	$v_R/v_S, A_S^{(1)}$ Fourier 10 yr	Petigura <sup>(2)</sup> Photodyn 3.3 yr	From Radii <sup>(3)</sup>
$m_b$	$M_\oplus$	<b><math>30.8 \pm 1.3</math></b>	<b><math>29.62</math></b>	<b><math>30.03</math></b>	<b><math>32.4 \pm 1.7</math></b>	39.6
$m_c$	$M_\oplus$	<b><math>11.12 \pm 0.44</math></b>	<b><math>10.94</math></b>	<b><math>11.08</math></b>	<b><math>10.8 \pm 0.6</math></b>	18.0
$\Delta m_{b,c}/m_{b,c}$			-0.04, -0.02	-0.02, -0.004	+0.05, +0.03	+0.29, +0.62
$\rho_b$	$\text{g cm}^{-3}$	0.59	0.57	0.58	0.52	0.76
$\rho_c$	$\text{g cm}^{-3}$	1.05	1.03	1.04	0.86	1.69
$P_S (\bar{P}_S)$	d			2711.2		(2751.9)
$P_R$	d			717.4		
$A_S^{(b)}, A_R^{(b)}$	min			53.4, (41.7)		
$A_S^{(c)}, A_R^{(c)}$	min			233.2, (148.3)		
$\beta_S, \beta_R$	deg	$[78.1]_{-1.4}^{+1.5}$ [137.3] $_{-1.9}^{+2.2}$	[76.1], [138.1]	(76.5, 144.3)		
$\lambda_n$	deg	$85.8_{-1.9}^{+1.7}$	82.8		37.5 <sup>(4)</sup>	
$R$		$[14.81]_{-0.26}^{+0.37}$	[15.49]	13.28	[15.7]	
$\Delta\sigma$		$[0.0029]_{-2.e-5}^{+1.e-5}$	[0.0029]	0.0030	[0.0029]	
$e_b^{(+)} (e_b)$		$[0.015]_{-0.002}^{+0.0002}$ (0.043) $_{-0.024}^{+0.024}$	[0.015] (0.069)	0.015	[0.015] (0.20) $_{-0.03}^{+0.03}$	
$e_c^{(+)} (e_c)$		$[0.044]_{-0.004}^{+0.0005}$ (0.067) $_{-0.017}^{+0.017}$	[0.045] (0.078)	0.043	[0.047] (0.21) $_{-0.03}^{+0.03}$	

**Notes.**(1):  $v_R/v_S, A_S$  / Fourier A uses the frequency ratio and superamplitudes only to estimate masses;

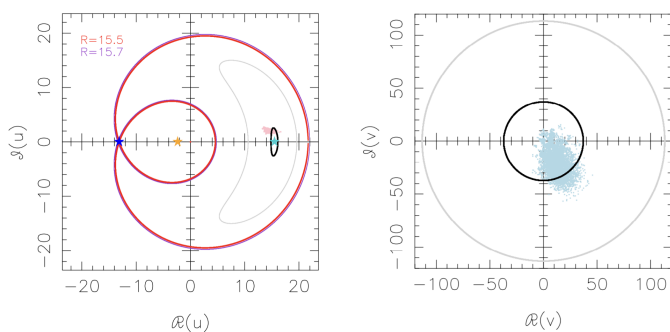
(2): Petigura / Photodyn uses system parameters from the photodynamical analysis of Petigura et al. (2020);

(3): Estimates using mass-radius relation  $m_p/M_E = (R_p/0.56 R_E)^{1/0.67}$  (Müller et al. 2024);(4): Petigura et al. (2020) value minus 180° to account for the fact that the authors assumed  $\Omega_b(t_{\text{ref}}) = 0$ ;

[Square brackets] show the quantity calculated analytically from elements and masses using the formalism of Mardling (2025a);

 $\Delta m_{b,c}/m_{b,c}$  = relative difference in masses compared to median value; $\bar{P}_S$  (defined from ephemeris periods such that  $\bar{P}_S^{-1} = n\bar{P}_b^{-1} - (n+1)\bar{P}_c^{-1}$ ) listed in the last column for comparison with the Fourier superperiod;**Boldface entries:** highlighted for comparison;

Amplitudes and phases in brackets were not used directly in mass estimates.

Last two rows: Entries in brackets are the median and 68.3% CI eccentricities for comparison with the fixed-point values  $e_b^{(+)}$  and  $e_c^{(+)}$ .The reference mean densities are  $\rho_{\text{Saturn}} = 0.69 \text{ g cm}^{-3}$ ,  $\rho_{\text{Uranus}} = 1.15 \text{ g cm}^{-3}$ .

**Fig. 8.** Phase space in which K2-19 b,c reside. *Left panel:* Our posterior values of the real and imaginary parts of  $u$  (7000 pink points) using Eq. (6); a complete resonant cycle starting from the MAP value of  $u$  (black curve); the associated primary fixed point for which  $u = R$  (cyan star) and the secondary and hyperbolic fixed points (orange and blue stars, respectively, these two only exist when the phase space is resonant); the associated separatrix (red curve); a complete resonant cycle using the system parameters of Petigura et al. (2020) for the initial value of  $u$  (gray curve); and the associated separatrix, which is almost identical to ours (purple curve). *Right panel:* Our posterior values of the real and imaginary parts of  $v$  (7000 light blue points) using Eq. (7); a complete supercycle starting from the MAP value of  $v$  (black curve) and the system parameters of Petigura et al. (2020) (gray curve). Each panel uses different scales.

### 5.6. Comparison with previous works

The first photodynamical analysis of K2-19 with a time span of 285 days was presented by Barros et al. (2015). They found

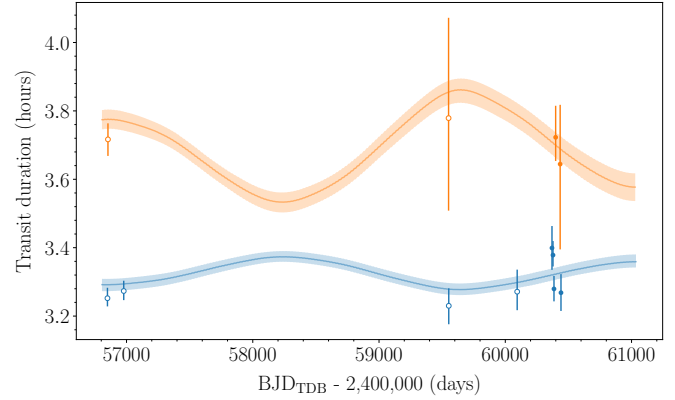


**Fig. 9.** Posterior of the transit duration of K2-19 b (blue band) and K2-19 c (orange band). We used 1000 random draws from the posterior distribution to estimate the median transit duration and its uncertainty (68.3% CI). The error bars represent the transit durations we measured for individual transits (filled dots) or groups of transits (open dots placed at the average timing of the transits) using the procedure described in Sect. B.

$e_b = 0.119_{-0.035}^{+0.082}$  and  $e_c = 0.095_{-0.035}^{+0.073}$  at 2456813 BJD<sub>TDB</sub>. These values are different by  $1.8\sigma$  ( $e_b$ ) and  $0.7\sigma$  ( $e_c$ ) from our results. Their mass ratios  $m_b/m_\star = (13.4_{-2.9}^{+4.3}) \times 10^{-5}$ ,  $m_c/m_\star = (5.5_{-1.3}^{+2.0}) \times 10^{-5}$ , and  $m_c/m_b = 0.42 \pm 0.12$  agree with our results with differences of  $1.0\sigma$ ,  $1.3\sigma$ , and  $0.5\sigma$ , respectively.

The next photodynamical analysis of K2-19 was performed by Petigura et al. (2020) with a time span of 3.3 years. They

obtained osculating  $e_b = 0.20 \pm 0.03$ ,  $e_c = 0.21 \pm 0.03$ , and well-aligned apsides ( $\omega_c - \omega_b = 2 \pm 2^\circ$ ). We did not find the reference time for the orbital parameters in Petigura et al. (2020). Assuming that their reference time is close to ours, the difference from our result is  $4.1\sigma$  for both planets, which cannot be explained by orbital evolution if the reference time was significantly different from ours. Despite the differences in eccentricities, their masses of K2-19 b and c agree with our results (for the reasons explained in Sect. 5.3). Based on the difference between the transit times predicted by Petigura et al. (2020) and those observed (Fig. C.4), which are up to  $6.7\sigma$  and 14 hours, we suspect an issue in their analysis. As shown in Sect. C, K2-19 d and e cannot have caused this discrepancy, and neither can the shorter time span of the observations. Perhaps the discrepant individual timing they found for the LCOGT partial transit ( $3.5\sigma$  off based on our results) has driven their solution. As shown in Fig. 6 of Petigura et al. (2020), their model already struggled to fit this transit timing. When Petit et al. (2020) enforced a low-eccentricity solution, the model for the LCOGT timing fell at the same value as we found, which corresponds to  $12.4 \pm 0.9$  minutes in the residuals of Fig. 7 in Petit et al. (2020).

We briefly compare our results with the analyses that only used radial velocities from Dai et al. (2016) and Nespral et al. (2017). Dai et al. (2016) found radial velocity amplitudes of  $K_b = 9.6_{-1.6}^{+1.8} \text{ m s}^{-1}$  and  $K_c = 7.5 \pm 2.1 \text{ m s}^{-1}$ , which differ by  $0.6\sigma$  and  $2.0\sigma$ , respectively, from our results. On the other hand, Nespral et al. (2017) found  $K_b = 18.8 \pm 2.4 \text{ m s}^{-1}$ , which differs by  $3.4\sigma$  from our results, and did not significantly detect K2-19 c.

## 5.7. Internal structure

Internal structure retrieval is especially degenerate for gas giants. Petigura et al. (2020) used the models of Lopez & Fortney (2014) and found that K2-19 b has a hydrogen-helium envelope mass fraction of  $f_{\text{env}} = 44 \pm 3\%$  by mass, which challenges the core-accretion theory. Runaway accretion begins at about  $f_{\text{env}} \approx 50\%$ , and fine-tuning would be required for the disk to disappear at just the moment when K2-19 b approached the runaway phase.

We followed Castro-González et al. (2024b) and investigated the internal structure of K2-19 b using GASTLI (Acuña et al. 2021, 2024), which is a one-dimensional coupled interior-atmosphere model for warm ( $T_{\text{eq}} < 1000 \text{ K}$ ) gas giants (between  $17 M_E$  and  $6 M_J$ ). The interior model is composed of two layers, that is, the core and the envelope. The core is assumed to be a 1:1 mixture of silicate rock and water, whereas the envelope is a mixture of H/He and water. The model is parameterized with two values: the core mass fraction (CMF) and the mass fraction of water (representative of metals) in the envelope ( $Z_{\text{env}}$ ).

We generated a grid of GASTLI models for  $T_{\text{eq}} = 857 \text{ K}$ ,  $\text{C/O}=0.55$  (solar value), masses from  $24$  to  $38 M_E$  with increments of  $0.25 M_E$ , a CMF from  $0$  to  $0.99$  with increments of  $0.1$ ,  $\log(\text{Fe/H})$  from  $-2$  to  $2.4$  with increments of  $0.5$ , and  $T_{\text{int}}$  from  $50$  to  $250 \text{ K}$  with increments of  $25 \text{ K}$ . For the retrieval, we used the planetary mass and radius and the stellar age as observable parameters. We sampled from the posterior distribution with emcee (Goodman & Weare 2010; Foreman-Mackey et al. 2013). The interior parameter priors and posteriors are listed in Table 6. The one- and two-dimensional projections of the posterior sample (Foreman-Mackey 2016) of selected system parameters are shown in Fig. A.11. The envelope mass fraction ( $f_{\text{env}}$  for Lopez & Fortney 2014) is  $0.283_{-0.049}^{+0.038}$ . The total water (metals) mass fraction is  $Z_{\text{planet}} = 0.729_{-0.14}^{+0.041}$ . We compared our results with those by Thorngren et al. (2016). We computed the stellar metal

**Table 6.** Interior structure retrieval of K2-19 b with GASTLI.

Parameter	Prior	Posterior median and $68.3\%$ CI
Core mass fraction, CMF	$U(0.01, 0.99)$	$0.718_{-0.38}^{+0.049}$
Atmospheric metallicity, $\log(\text{Fe/H})$	$U(-2, 2.4)$	$0.4_{-1.6}^{+1.1}$
Envelope water mass fraction, $Z_{\text{env}}$		$0.054_{-0.049}^{+0.31}$
Total water mass fraction, $Z_{\text{planet}}$		$0.729_{-0.14}^{+0.041}$
Internal temperature, $T_{\text{int}}$ ( $\text{K}$ )	$U(50, 200)$	$98.8_{-13}^{+8.6}$

Notes.  $U(l,u)$ : Uniform distribution prior in the range [l, u].

mass fraction as  $Z_\star = 0.014 \times 10^{[\text{Fe}/\text{H}]_\star}$  to infer the heavy-element enrichment relative to the host star:  $Z_{\text{planet}}/Z_\star = 48.1_{-8.8}^{+4.1}$ . This value is compatible with formation via core accretion for a planet mass of  $0.0968 \pm 0.0039 M_J$  (see Fig. 11 of Thorngren et al. 2016).

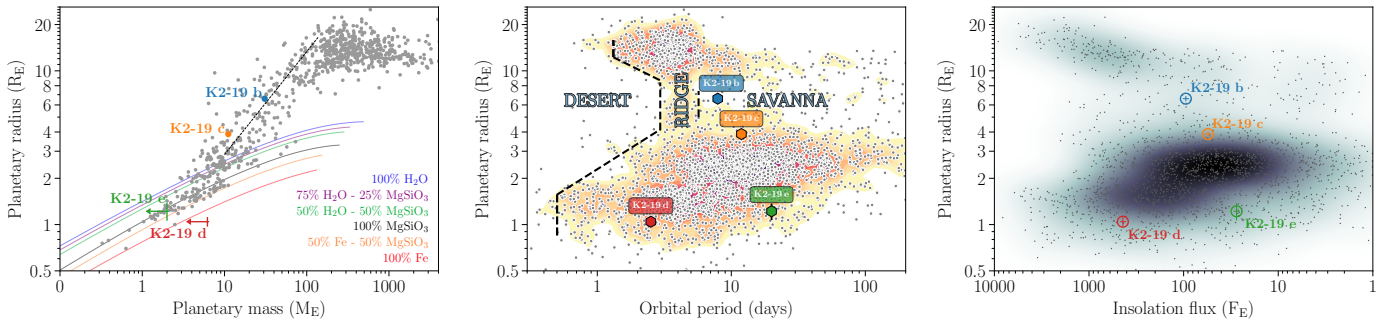
## 6. Discussion

Figure 10 illustrates that K2-19 b and c lie within the Neptune savanna (Bourrier et al. 2023), which is a moderately populated region in the period–radius diagram that is found at orbital periods longer than those that define the Neptune desert (e.g., Lecavelier des Etangs 2007; Mazeh et al. 2016) and the Neptunian ridge (Castro-González et al. 2024a). Both planets exhibit low densities ( $0.590 \pm 0.053 \text{ g cm}^{-3}$  and  $1.046 \pm 0.097 \text{ g cm}^{-3}$  for K2-19 b and K2-19 c, respectively), as anticipated for the planets in the savanna (Castro-González et al. 2024b). K2-19 c satisfies the selection criteria of the sample defined by Leleu et al. (2024), which supports their finding that resonant sub-Neptunes tend to be puffier.

The 3:2 mean-motion resonance is one of the most common configurations observed in known multiplanetary systems (Dai et al. 2024). This resonance is thought to be particularly robust, to often act as the first capture point for migrating planets, and to provide long-term dynamical stability. The updated orbital parameters of the K2-19 system are broadly consistent with a disk-driven migration scenario. The nonzero free eccentricity suggests, however, that an additional excitation mechanism must have operated during or after migration. The system is part of the ATREIDES spin-orbit angle survey (Bourrier et al. 2025), which will bring further constraints on the 3D orbital architecture of the planets and their dynamical origin.

The precision on the planet-to-star mass ratio is  $0.8\%$  for planet b and  $1.5\%$  for planet c, and the masses have a relative precision of  $4.2\%$  for planet b and  $4.0\%$  for planet c, which are dominated by the  $3.8\%$  uncertainty on the stellar mass. The two well-separated periodicities in the TTVs (super and resonant) enables a robust determination of the planetary masses independent of the eccentricities. In contrast, constraints on the free eccentricities are weak because an inherent degeneracy is associated with low-eccentricity two-planet systems, and the libration and/or circulation behavior of the usual resonance angles and difference in the longitudes of periastron is similarly degenerate. Thus, while future transit observations aimed at refining the system architecture should prioritize epochs with the largest predicted timing uncertainties, these observations are unlikely to constrain the free eccentricities much more than they are at present.

Although faint ( $J=11.6$  mag), K2-19 b has a transmission spectroscopy metric (TSM; Kempton et al. 2018) of  $64.8 \pm 4.5$ , which is among the ten most favorable planets of this size ( $6\text{-}7 R_E$ ) with an equilibrium temperature below  $1000 \text{ K}$ . The James Webb Space Telescope (Gardner et al. 2006) might be able to



**Fig. 10.** Comparison of the K2-19 planets with known exoplanets. *Left:* Mass–radius diagram of known exoplanets. The gray dots show the transiting planets listed in the NASA Exoplanet Archive (<https://exoplanetarchive.ipac.caltech.edu/>, Akeson et al. 2013) with planetary radius and mass uncertainties below 20%. The dashed black line shows the sub-Neptune mass–radius relation from Parc et al. (2024). The solid lines represent theoretical models for different compositions (Zeng & Sasselov 2013). *Center:* Idem for planetary radii vs. orbital period (restricted to planets with planetary radius uncertainties below 20%), with exo-Neptunian boundaries from Castro-González et al. (2024a). *Right:* Idem for planetary radii vs. insolation flux. A Gaussian kernel density estimate is shown in different color intensities.

measure the metallicity of the atmosphere of K2-19 b and place an additional constraint on the planet interior.

Petigura et al. (2020) used photodynamical modeling for K2 data, but only transit timing for the other observations. As we showed in Sect. C, the likely cause of their high retrieved eccentricities is a single timing from a partial transit near the end of the transit-timing dataset that was miscalculated ( $3.5\sigma$ , or  $12.4 \pm 3.6$  minutes, off). This highlights the susceptibility of the results to single outliers when the available data are barely enough to constrain the solution. In this case, using a photodynamical model for all observations might have enabled a better error propagation and avoided an overestimation of the eccentricities in the past.

## Data availability

Light curves, samples from the posterior, and transit times forecast up to the year 2035 can be found at <https://zenodo.org/records/17084030>.

**Acknowledgements.** We are grateful to the ESO/La Silla staff for their continuous support of ExTrA. We acknowledge funding from the European Research Council under the ERC Grant Agreement n. 337591-ExTrA. CHEOPS is an ESA mission in partnership with Switzerland with important contributions to the payload and the ground segment from Austria, Belgium, France, Germany, Hungary, Italy, Portugal, Spain, Sweden, and the United Kingdom. The CHEOPS Consortium would like to gratefully acknowledge the support received by all the agencies, offices, universities, and industries involved. Their flexibility and willingness to explore new approaches were essential to the success of this mission. CHEOPS data analyzed in this article will be made available in the CHEOPS mission archive ([https://cheops.unige.ch/archive\\_browser/](https://cheops.unige.ch/archive_browser/)). This paper includes data collected by the TESS mission. Funding for the TESS mission is provided by the NASA’s Science Mission Directorate. We acknowledge the use of public TESS data from pipelines at the TESS Science Office and at the TESS Science Processing Operations Center. Resources supporting this work were provided by the NASA High-End Computing (HEC) Program through the NASA Advanced Supercomputing (NAS) Division at Ames Research Center for the production of the SPOC data products. This paper includes data collected by the TESS mission that are publicly available from the Mikulski Archive for Space Telescopes (MAST). This paper includes data collected by the Kepler mission and obtained from the MAST data archive at the Space Telescope Science Institute (STScI). Funding for the Kepler mission is provided by the NASA Science Mission Directorate. STScI is operated by the Association of Universities for Research in Astronomy, Inc., under NASA contract NAS 5-26555. This work makes use of observations from the Las Cumbres Observatory global telescope network. We thank the Swiss National Science Foundation (SNSF) and the Geneva University for their continuous support to our planet search programs. This work has been carried out within the framework of the National Centre of Competence in Research PlanetS supported by the Swiss National Science Foundation under grants 51NF40\_182901 and 51NF40\_205606. The authors acknowledge the financial support of the

SNSF. This publication makes use of data products from the Two Micron All Sky Survey, which is a joint project of the University of Massachusetts and the Infrared Processing and Analysis Center/California Institute of Technology, funded by the National Aeronautics and Space Administration and the National Science Foundation. This publication makes use of data products from the Wide-field Infrared Survey Explorer, which is a joint project of the University of California, Los Angeles, and the Jet Propulsion Laboratory/California Institute of Technology, funded by the National Aeronautics and Space Administration. This work has made use of data from the European Space Agency (ESA) mission *Gaia* (<https://www.cosmos.esa.int/gaia>), processed by the *Gaia* Data Processing and Analysis Consortium (DPAC, <https://www.cosmos.esa.int/web/gaia/dpac/consortium>). Funding for the DPAC has been provided by national institutions, in particular the institutions participating in the *Gaia* Multilateral Agreement. Simulations in this paper made use of the REBOUND code which can be downloaded freely at <http://github.com/hannorein/rebound>. This research made use of nep-des (available in <https://github.com/castro-gzlx/nep-des>). Part of these simulations have been run on the *Lesta* and *Bonsai* clusters kindly provided by the Observatoire de Genève. This project has received funding from the European Research Council (ERC) under the European Union’s Horizon 2020 research and innovation programme (project SPICE DUNE, grant agreement No 947634). M.L. acknowledges support of the Swiss National Science Foundation under grant number PCEFP2\_194576. I.G.J. acknowledges support of the National Science and Technology Council in Taiwan under grant number NSTC 113-2112-M-007-030. We acknowledge grants Spanish program Unidad de Excelencia María de Maeztu CEX2020-001058-M and 2021-SGR-1526 (Generalitat de Catalunya). In addition to the Python packages mentioned in the text, we utilized NumPy (Harris et al. 2020), SciPy (Virtanen et al. 2020), matplotlib (Hunter 2007), and seaborn (Waskom 2021).

## References

- Acuña, L., Deleuil, M., Mousis, O., et al. 2021, A&A, 647, A53
- Acuña, L., Kreidberg, L., Zhai, M., & Mollière, P. 2024, A&A, 688, A60
- Agol, E., Steffen, J., Sari, R., & Clarkson, W. 2005, MNRAS, 359, 567
- Akeson, R. L., Chen, X., Ciardi, D., et al. 2013, PASP, 125, 989
- Allard, F., Homeier, D., & Freytag, B. 2012, Philosophical Transactions of the Royal Society of London Series A, 370, 2765
- Almenara, J. M., Díaz, R. F., Dorn, C., Bonfils, X., & Udry, S. 2018, MNRAS, 478, 460
- Andrae, R., Fouesneau, M., Sordo, R., et al. 2023, A&A, 674, A27
- Armstrong, D. J., Santerne, A., Veras, D., et al. 2015, A&A, 582, A33
- Astropy Collaboration, Price-Whelan, A. M., Lim, P. L., et al. 2022, ApJ, 935, 167
- Astropy Collaboration, Price-Whelan, A. M., Sipőcz, B. M., et al. 2018, AJ, 156, 123
- Astropy Collaboration, Robitaille, T. P., Tollerud, E. J., et al. 2013, A&A, 558, A33
- Barnes, S. A. 2010, ApJ, 722, 222
- Barnes, S. A. & Kim, Y.-C. 2010, ApJ, 721, 675
- Barros, S. C. C., Almenara, J. M., Demangeon, O., et al. 2015, MNRAS, 454, 4267
- Benz, W., Broeg, C., Fortier, A., et al. 2021, Experimental Astronomy, 51, 109
- Bitsch, B., Crida, A., Libert, A. S., & Lega, E. 2013, A&A, 555, A124

- Bonfils, X., Almenara, J. M., Jocou, L., et al. 2015, in Society of Photo-Optical Instrumentation Engineers (SPIE) Conference Series, Vol. 9605, Techniques and Instrumentation for Detection of Exoplanets VII, ed. S. Shaklan, 96051L
- Borucki, W. J., Koch, D., Basri, G., et al. 2010, *Science*, 327, 977
- Bourrier, V., Attia, O., Mallonn, M., et al. 2023, *A&A*, 669, A63
- Bourrier, V., Steiner, M., Castro-González, A., et al. 2025, *A&A*, 701, A190
- Bradley, L. 2023, *astropy/photutils*: 1.8.0
- Brandeker, A., Patel, J. A., & Morris, B. M. 2024, PIPE: Extracting PSF photometry from CHEOPS data, *Astrophysics Source Code Library*, record ascl:2404.002
- Brewer, J. M., Fischer, D. A., Valenti, J. A., & Piskunov, N. 2016, *ApJS*, 225, 32
- Broeg, C., Fernández, M., & Neuhauser, R. 2005, *Astronomische Nachrichten*, 326, 134
- Brown, T. M., Baliber, N., Bianco, F. B., et al. 2013, *Publications of the Astronomical Society of the Pacific*, 125, 1031
- Carter, J. A., Fabrycky, D. C., Ragozzine, D., et al. 2011, *Science*, 331, 562
- Castro-González, A., Bourrier, V., Lillo-Box, J., et al. 2024a, *A&A*, 689, A250
- Castro-González, A., Lillo-Box, J., Armstrong, D. J., et al. 2024b, *A&A*, 691, A233
- Chen, Y., Girardi, L., Bressan, A., et al. 2014, *MNRAS*, 444, 2525
- Choksi, N. & Chiang, E. 2023, *MNRAS*, 522, 1914
- Claytor, Z. R., van Saders, J. L., Santos, Á. R. G., et al. 2020, *ApJ*, 888, 43
- Cresswell, P. & Nelson, R. P. 2008, *A&A*, 482, 677
- Cutri, R. M., Skrutskie, M. F., van Dyk, S., et al. 2003, *VizieR Online Data Catalog*, II/246
- Cutri, R. M., Wright, E. L., Conrow, T., et al. 2021, *VizieR Online Data Catalog: AllWISE Data Release (Cutri+ 2013)*, *VizieR On-line Data Catalog*, II/328. Originally published in: IPAC/Caltech (2013)
- Dai, F., Goldberg, M., Batygin, K., et al. 2024, *AJ*, 168, 239
- Dai, F., Winn, J. N., Albrecht, S., et al. 2016, *ApJ*, 823, 115
- Deck, K. M., Agol, E., Holman, M. J., & Nesvorný, D. 2014, *ApJ*, 787, 132
- Díaz, R. F., Almenara, J. M., Santerne, A., et al. 2014, *MNRAS*, 441, 983
- Dotter, A., Chaboyer, B., Jevremović, D., et al. 2008, *ApJS*, 178, 89
- Espinosa, N., Kossakowski, D., & Brahm, R. 2019, *MNRAS*, 490, 2262
- Fabrycky, D. C., Lissauer, J. J., Ragozzine, D., et al. 2014, *ApJ*, 790, 146
- Foreman-Mackey, D. 2016, *The Journal of Open Source Software*, 1, 24
- Foreman-Mackey, D., Agol, E., Ambikasaran, S., & Angus, R. 2017, *AJ*, 154, 220
- Foreman-Mackey, D., Hogg, D. W., Lang, D., & Goodman, J. 2013, *PASP*, 125, 306
- Foreman-Mackey, D., Montet, B. T., Hogg, D. W., et al. 2015, *ApJ*, 806, 215
- Gaia Collaboration, Prusti, T., de Bruijne, J. H. J., et al. 2016, *A&A*, 595, A1
- Gaia Collaboration, Vallenari, A., Brown, A. G. A., et al. 2023, *A&A*, 674, A1
- García, L. J., Foreman-Mackey, D., Murray, C. A., et al. 2024, *AJ*, 167, 284
- García, L. J., Timmermans, M., Pozuelos, F. J., et al. 2022, *MNRAS*, 509, 4817
- Gardner, J. P., Mather, J. C., Clampin, M., et al. 2006, *Space Sci. Rev.*, 123, 485
- Goldberg, M. & Batygin, K. 2023, *ApJ*, 948, 12
- Goodman, J. & Weare, J. 2010, *Communications in applied mathematics and computational science*, 5, 65
- Gregory, P. C. 2005, *ApJ*, 631, 1198
- Hardegree-Ullman, K. K., Zink, J. K., Christiansen, J. L., et al. 2020, *ApJS*, 247, 28
- Harris, C. R., Millman, K. J., van der Walt, S. J., et al. 2020, *Nature*, 585, 357
- Holman, M. J. & Murray, N. W. 2005, *Science*, 307, 1288
- Hoyer, S., Guterman, P., Demangeon, O., et al. 2020, *A&A*, 635, A24
- Huber, D., Bryson, S. T., Haas, M. R., et al. 2016, *ApJS*, 224, 2
- Huber, D., Carter, J. A., Barbieri, M., et al. 2013, *Science*, 342, 331
- Hunter, J. D. 2007, *Computing in Science & Engineering*, 9, 90
- Irwin, J. B. 1952, *ApJ*, 116, 211
- Izidoro, A., Ogihara, M., Raymond, S. N., et al. 2017, *MNRAS*, 470, 1750
- Jenkins, J. M., Twicken, J. D., McCauliff, S., et al. 2016, in Society of Photo-Optical Instrumentation Engineers (SPIE) Conference Series, Vol. 9913, Software and Cyberinfrastructure for Astronomy IV, 99133E
- Kass, R. E. & Raftery, A. E. 1995, *Journal of the American Statistical Association*, 90, 773
- Kempton, E. M. R., Bean, J. L., Louie, D. R., et al. 2018, *PASP*, 130, 114401
- Kipping, D. M. 2010, *MNRAS*, 408, 1758
- Kipping, D. M. 2013, *MNRAS*, 435, 2152
- Kreidberg, L. 2015, *PASP*, 127, 1161
- Laune, J. T., Rodet, L., & Lai, D. 2022, *MNRAS*, 517, 4472
- Lecavelier des Etangs, A. 2007, *A&A*, 461, 1185
- Leleu, A., Delisle, J.-B., Burn, R., et al. 2024, *A&A*, 687, L1
- Lendl, M. 2014, PhD thesis, University of Geneva, Switzerland
- Lendl, M., Anderson, D. R., Collier-Cameron, A., et al. 2012, *A&A*, 544, A72
- Lindgren, L., Klioner, S. A., Hernández, J., et al. 2021, *A&A*, 649, A2
- Lithwick, Y., Xie, J., & Wu, Y. 2012, *ApJ*, 761, 122
- Lopez, E. D. & Fortney, J. J. 2014, *ApJ*, 792, 1
- Luger, R., Agol, E., Kruse, E., et al. 2016, *AJ*, 152, 100
- Luger, R., Kruse, E., Foreman-Mackey, D., Agol, E., & Saunders, N. 2018, *AJ*, 156, 99
- Magrini, L., Danielski, C., Bossini, D., et al. 2022, *A&A*, 663, A161
- Mandel, K. & Agol, E. 2002, *ApJ*, 580, L171
- Manduca, A., Bell, R. A., & Gustafsson, B. 1977, *A&A*, 61, 809
- Mazeh, T., Holczer, T., & Faigler, S. 2016, *A&A*, 589, A75
- McCully, C., Volgenau, N. H., Harbeck, D.-R., et al. 2018, in Society of Photo-Optical Instrumentation Engineers (SPIE) Conference Series, Vol. 10707, Software and Cyberinfrastructure for Astronomy V, ed. J. C. Guzman & J. Ibsen, 107070K
- McQuillan, A., Aigrain, S., & Mazeh, T. 2013, *MNRAS*, 432, 1203
- Meibom, S., Barnes, S. A., Platais, I., et al. 2015, *Nature*, 517, 589
- Montet, B. T., Morton, T. D., Foreman-Mackey, D., et al. 2015, *ApJ*, 809, 25
- Müller, S., Baron, J., Helled, R., Bouchy, F., & Parc, L. 2024, *A&A*, 686, A296
- Narita, N., Hirano, T., Fukui, A., et al. 2015, *ApJ*, 815, 47
- Nascimbeni, V., Borsato, L., Leonardi, P., et al. 2024, *A&A*, 690, A349
- Nespal, D., Gandolfi, D., Deeg, H. J., et al. 2017, *A&A*, 601, A128
- Nesvorný, D. & Vokrouhlický, D. 2016, *ApJ*, 823, 72
- Parc, L., Bouchy, F., Venturini, J., Dorn, C., & Helled, R. 2024, *A&A*, 688, A59
- Pecaut, M. J. & Mamajek, E. E. 2013, *ApJS*, 208, 9
- Petigura, E. A., Livingston, J., Batygin, K., et al. 2020, *AJ*, 159, 2
- Petit, A. C., Petigura, E. A., Davies, M. B., & Johansen, A. 2020, *MNRAS*, 496, 3101
- Rein, H. & Liu, S. F. 2012, *A&A*, 537, A128
- Rein, H. & Tamayo, D. 2015, *MNRAS*, 452, 376
- Ricker, G. R., Winn, J. N., Vanderspek, R., et al. 2015, *Journal of Astronomical Telescopes, Instruments, and Systems*, 1, 014003
- Riello, M., De Angelis, F., Evans, D. W., et al. 2021, *A&A*, 649, A3
- Rubin, D. B. 1987, *Journal of the American Statistical Association*, 82, 543
- Sinukoff, E., Howard, A. W., Petigura, E. A., et al. 2016, *ApJ*, 827, 78
- Skrutskie, M. F., Cutri, R. M., Stiening, R., et al. 2006, *AJ*, 131, 1163
- Smith, J. C., Stumpe, M. C., Van Cleve, J. E., et al. 2012, *PASP*, 124, 1000
- Sousa, S. G., Adibekyan, V., Delgado-Mena, E., et al. 2018, *A&A*, 620, A58
- Sousa, S. G., Adibekyan, V., Delgado-Mena, E., et al. 2021, *A&A*, 656, A53
- Speagle, J. S. 2020, *MNRAS*, 493, 3132
- Stassun, K. G., Oelkers, R. J., Paegert, M., et al. 2019, *AJ*, 158, 138
- Stassun, K. G., Oelkers, R. J., Pepper, J., et al. 2018, *AJ*, 156, 102
- Stumpe, M. C., Smith, J. C., Catanzarite, J. H., et al. 2014, *PASP*, 126, 100
- Stumpe, M. C., Smith, J. C., Van Cleve, J. E., et al. 2012, *PASP*, 124, 985
- Su, T., Zhang, L.-y., Long, L., et al. 2022, *ApJS*, 261, 26
- Taylor, J., Claytor, Z. R., Huber, D., & van Saders, J. 2022, *ApJ*, 927, 31
- Teske, J. K., Thorngren, D., Fortney, J. J., Hinkel, N., & Brewer, J. M. 2019, *AJ*, 158, 239
- Thorngren, D. P., Fortney, J. J., Murray-Clay, R. A., & Lopez, E. D. 2016, *ApJ*, 831, 64
- Vanderburg, A., Latham, D. W., Buchhave, L. A., et al. 2016, *ApJS*, 222, 14
- Virtanen, P., Gommers, R., Oliphant, T. E., et al. 2020, *Nature Methods*, 17, 261
- Wang, R., Luo, A. L., Zhang, S., et al. 2023, *ApJS*, 266, 40
- Waskom, M. L. 2021, *Journal of Open Source Software*, 6, 3021
- Wright, E. L., Eisenhardt, P. R. M., Mainzer, A. K., et al. 2010, *AJ*, 140, 1868
- Xiong, S., Li, X., & Liao, C. 2022, *ApJS*, 261, 36
- Zeng, L. & Sasselov, D. 2013, *PASP*, 125, 227
- Zink, J. K., Hardegree-Ullman, K. K., Christiansen, J. L., et al. 2023, *AJ*, 165, 262

<sup>1</sup> Observatoire de Genève, Département d’Astronomie, Université de Genève, Chemin Pegasi 51b, 1290 Versoix, Switzerland

<sup>2</sup> Univ. Grenoble Alpes, CNRS, IPAG, F-38000 Grenoble, France

<sup>3</sup> School of Physics & Astronomy, Monash University, Victoria, 3800, Australia

<sup>4</sup> Instituto Tecnológico de Buenos Aires (ITBA), Iguazú 341, Buenos Aires, CABA C1437, Argentina

<sup>5</sup> Instituto de Ciencias Físicas (ICIFI; CONICET), ECyT-UNSAM, Campus Miguelete, 25 de Mayo y Francia, (1650) Buenos Aires, Argentina

<sup>6</sup> Department of Physics and Institute of Astronomy, National Tsing-Hua University, Hsinchu 30013, Taiwan

<sup>7</sup> Institute of Computational and Modeling Science, National Tsing-Hua University, Hsinchu 30013, Taiwan

<sup>8</sup> College of Surveying and Geo-Informatics, Tongji University, Shanghai, 200092, People’s Republic of China

<sup>9</sup> Department of Physics and Astronomy, Vanderbilt University, Nashville, TN 37235, USA

<sup>10</sup> National Astronomical Research Institute of Thailand, Chiang Mai, 50180, Thailand

<sup>11</sup> SRON, Space Research Organisation Netherlands, Niels Bohrweg 4, NL-2333 CA, Leiden, The Netherlands

<sup>12</sup> NASA Ames Research Center, Moffett Field, CA 94035, USA

<sup>13</sup> Institute of Space Sciences (ICE, CSIC), Carrer de Can Magrans S/N, Campus UAB, Cerdanyola del Vallès, E-08193, Spain

<sup>14</sup> Institut d’Estudis Espacials de Catalunya (IEEC), 08860 Castelldefels (Barcelona), Spain

<sup>15</sup> Department of Astrophysical Sciences, Princeton University, NJ 08544, USA

## Appendix A: Additional figures and tables

**Table A.1.** Modeling of the SED.

Parameter	Prior	Posterior median and 68.3% CI
Effective temperature, $T_{\text{eff}}$	(K) $N(5350, 110)$	$5363 \pm 74$
Surface gravity, $\log g$	(cgs) $N(4.42, 0.06)$	$4.527 \pm 0.029$
Metallicity, $[\text{Fe}/\text{H}]_{\star}$	(dex) $N(0.03, 0.02)$	$0.026 \pm 0.019$
Distance	(pc) $N(296.9, 1.7)$	$297.2 \pm 1.7$
$E_{(\text{B}-\text{V})}$	(mag) $U(0, 3)$	$0.030^{+0.052}_{-0.023}$
Jitter Gaia	(mag) $U(0, 1)$	$0.169^{+0.24}_{-0.092}$
Jitter 2MASS	(mag) $U(0, 1)$	$0.057^{+0.090}_{-0.037}$
Jitter WISE	(mag) $U(0, 1)$	$0.042^{+0.10}_{-0.032}$
Mass, $m_{\star}$	( $M_{\odot}$ )	$0.885 \pm 0.034$
Radius, $R_{\star}$	( $R_{\odot}$ )	$0.845 \pm 0.017$
Density, $\rho_{\star}$	( $\text{g cm}^{-3}$ )	$2.06 \pm 0.16$
Isochronal age	(Gyr)	$4.8 \pm 4.3$
Luminosity	( $L_{\odot}$ )	$0.531 \pm 0.030$

**Notes.**  $N(\mu, \sigma)$ : Normal distribution prior with mean  $\mu$ , and standard deviation  $\sigma$ .  $U(l, u)$ : Uniform distribution prior in the range  $[l, u]$ .

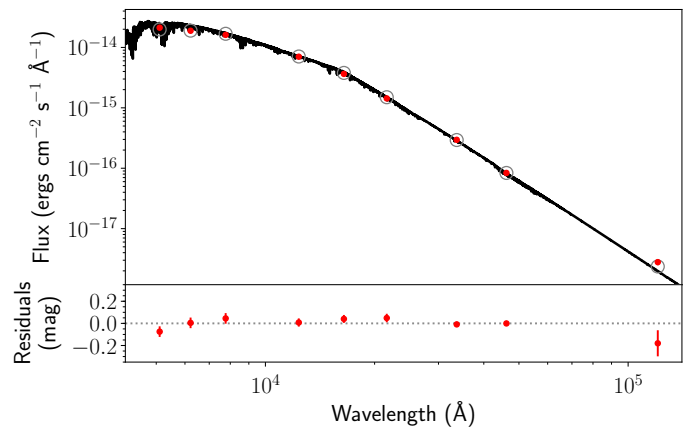


**Fig. A.1.** The SED of K2-19. *Top panel:* The solid line is the MAP PHOENIX/BT-Settl interpolated synthetic spectrum, red circles are the absolute photometric observations, and the open gray circles are the result of integrating the synthetic spectrum in the observed bandpasses. *Bottom panel:* Residuals of the MAP model (the jitter has been added quadratically to the data error bars).

**Table A.2.** Parameters of K2-19 from the literature.

Work	$T_{\text{eff}}$ (K)	$\log g$	$[\text{Fe}/\text{H}]_{\star}$	$[\text{M}/\text{H}]_{\star}$	$m_{\star}$ ( $M_{\odot}$ )	$R_{\star}$ ( $R_{\odot}$ )	d (pc)
Montet et al. (2015)	$5519^{+49}_{-82}$		$-0.27 \pm 0.10$		$0.84 \pm 0.04$	$0.81^{+0.09}_{-0.05}$	$291^{+33}_{-20}$
Armstrong et al. (2015)	$5230 \pm 420$	$4.39 \pm 0.79$	$0.38 \pm 0.23$		$0.92 \pm 0.14$	$1.03 \pm 0.20$	
Barros et al. (2015)	$5390 \pm 180$	$4.42 \pm 0.34$	$0.19 \pm 0.12$		$0.918^{+0.086}_{-0.070}$	$0.926^{+0.19}_{-0.069}$	
Narita et al. (2015)	$5345 \pm 17$	$4.394 \pm 0.050$	$0.07 \pm 0.03$		$0.902 \pm 0.011$	$0.914 \pm 0.027$	
Huber et al. (2016)	$5340 \pm 160$	$4.520 \pm 0.040$	$0.019^{+0.12}_{-0.080}$		$0.901^{+0.055}_{-0.031}$	$0.857^{+0.069}_{-0.054}$	$296^{+32}_{-29}$
Vanderburg et al. (2016)	$5391 \pm 50$	$4.60 \pm 0.10$		$-0.03 \pm 0.08$			
Sinukoff et al. (2016)	$5430 \pm 60$	$4.63 \pm 0.07$	$0.10 \pm 0.04$		$0.93 \pm 0.05$	$0.86 \pm 0.04$	
Brewer et al. (2016)	$5322 \pm 25$	$4.510 \pm 0.028$		$0.05 \pm 0.01$			
Nespral et al. (2017)	$5250 \pm 70$	$4.50 \pm 0.10$	$0.10 \pm 0.05$		$0.918 \pm 0.064$	$0.88 \pm 0.11$	
Sousa et al. (2018)	$5355 \pm 35$	$4.46 \pm 0.06$	$0.05 \pm 0.02$		$0.86 \pm 0.06$		
Stassun et al. (2018)	$5320 \pm 100$	$4.553 \pm 0.077$		$0.05 \pm 0.10$	$0.92 \pm 0.11$	$0.840 \pm 0.043$	$289.8 \pm 5.6$
Teske et al. (2019)	$5418 \pm 21$	$4.54 \pm 0.04$	$0.03 \pm 0.02$				
Hardegree-Ullman et al. (2020)	$5481 \pm 31$	$4.726 \pm 0.051$	$0.216 \pm 0.029$		$1.22^{+0.17}_{-0.15}$	$0.793^{+0.021}_{-0.020}$	$289.8^{+5.7}_{-5.5}$
Petigura et al. (2020)	$5320 \pm 100$	$4.51 \pm 0.08$	$0.06 \pm 0.05$		$0.88 \pm 0.03$	$0.82 \pm 0.03$	
Sousa et al. (2021)	$5346 \pm 27$	$4.42 \pm 0.06$	$0.03 \pm 0.02$		$0.846 \pm 0.006$	$0.864 \pm 0.028$	$299.3$
Magrini et al. (2022)	$5285 \pm 82$	$4.53 \pm 0.15$	$0.09 \pm 0.09$		$0.89^{+0.07}_{-0.11}$		
Su et al. (2022)	$5378 \pm 82$	$4.712 \pm 0.049$	$0.146 \pm 0.029$				
Xiong et al. (2022)	$5360 \pm 110$	$4.50 \pm 0.16$	$0.055 \pm 0.054$				
Andrae et al. (2023)	$5348^{+16}_{-20}$	$4.509^{+0.013}_{-0.015}$			$0.026^{+0.015}_{-0.018}$		$295.7^{+1.7}_{-1.6}$
Wang et al. (2023)	$5247 \pm 38$	$4.511 \pm 0.027$	$0.032 \pm 0.055$				
Zink et al. (2023)	$5420 \pm 100$	$4.55^{+0.01}_{-0.02}$	$0.14 \pm 0.06$		$0.91 \pm 0.02$	$0.84 \pm 0.01$	
This work (prior)		$4.531 \pm 0.044$			$0.885 \pm 0.034$	$0.845 \pm 0.039$	$296.9 \pm 1.7$
This work (posterior)		$4.556 \pm 0.024$			$0.892 \pm 0.034$	$0.824 \pm 0.024$	

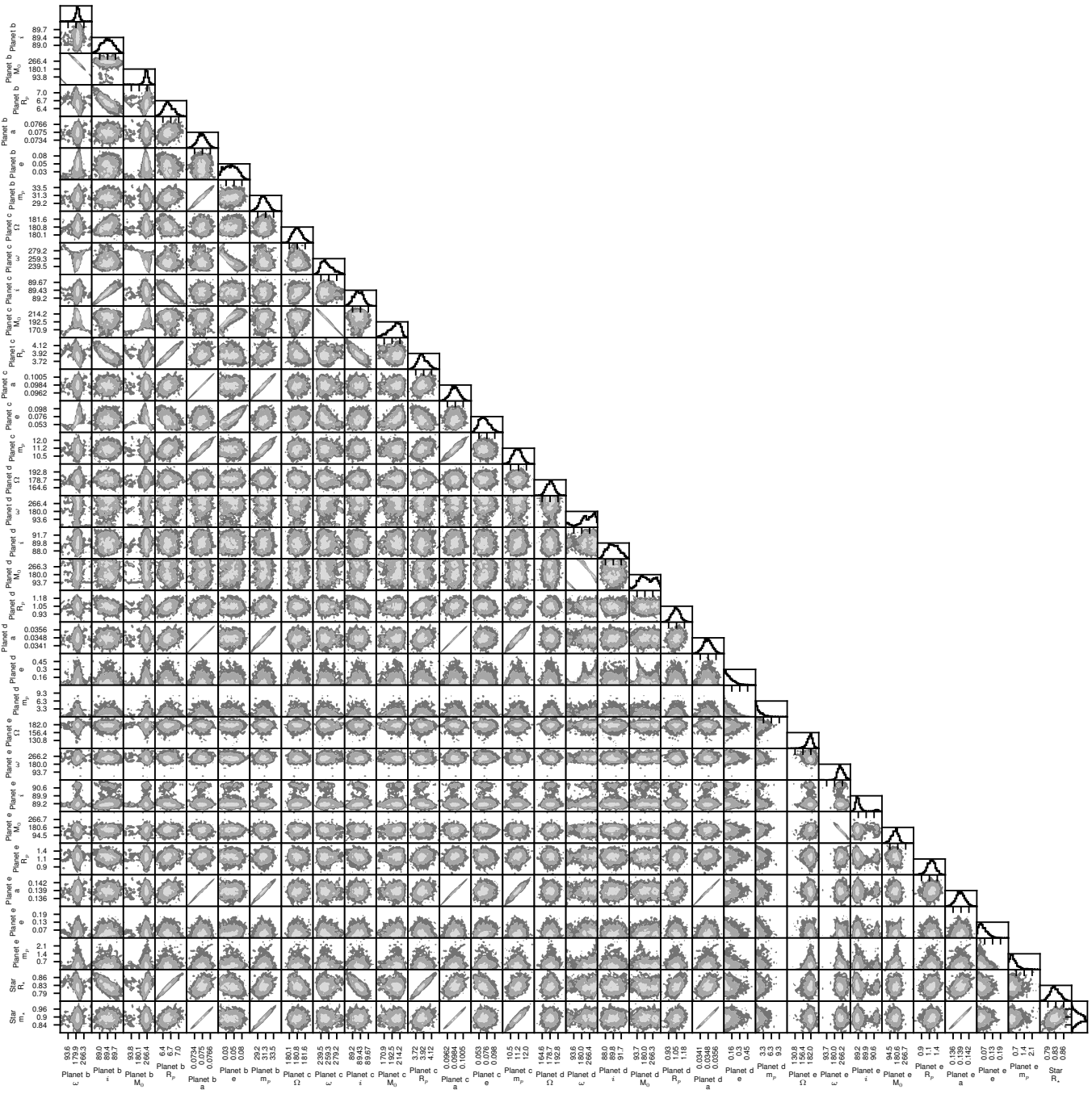


**Fig. A.2.** Two-parameter joint posterior distributions for the most relevant model parameters from the photodynamical modeling (Sect. 4.2). The 39.3, 68.3, and 95.4% two-variable joint confidence regions are denoted by three different gray levels; in the case of a Gaussian posterior, these regions project on to the one-dimensional 1, 2, and 3  $\sigma$  intervals. The histogram of the marginal distribution for each parameter is shown at the top of each column, except for the parameter on the last line, which is shown at the end of the line. Units are the same as in Table 4.

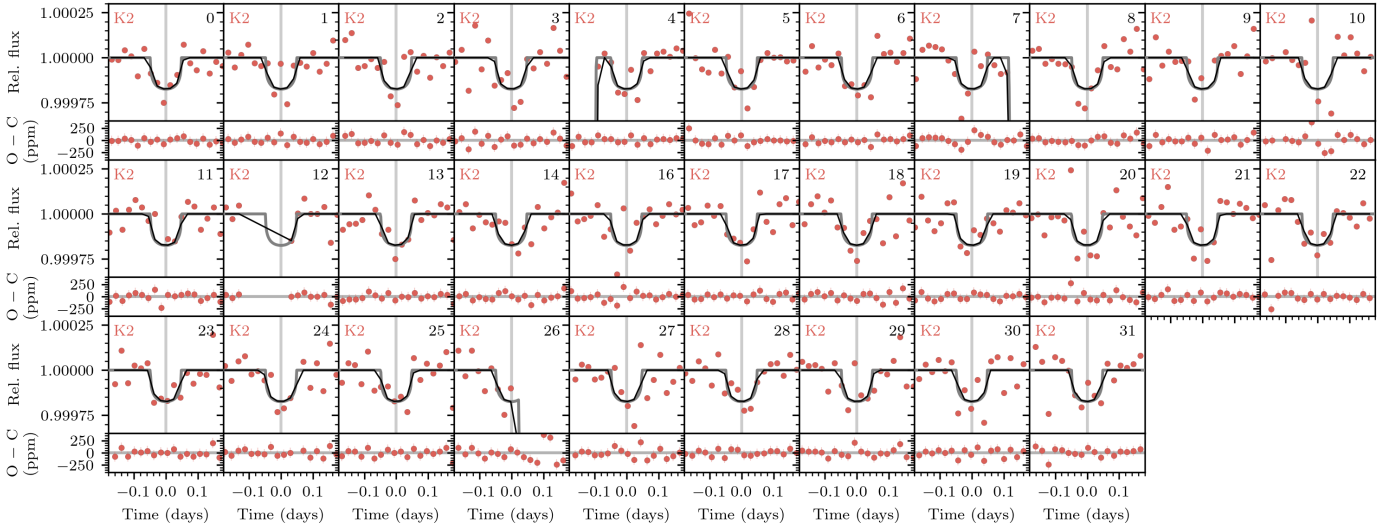


**Fig. A.3.** Noise-model-corrected transits of K2-19 d (dots with the same color code as in Fig. 2), the MAP model (black line), and the continuous oversampled MAP model (gray line) from the photodynamical modeling. Each panel is centered at the linear ephemeris (indicated by the vertical gray lines). Each panel is labeled with the telescopes that observed and the epoch number. The residuals after subtracting the MAP model are shown in the lower part of each panel.

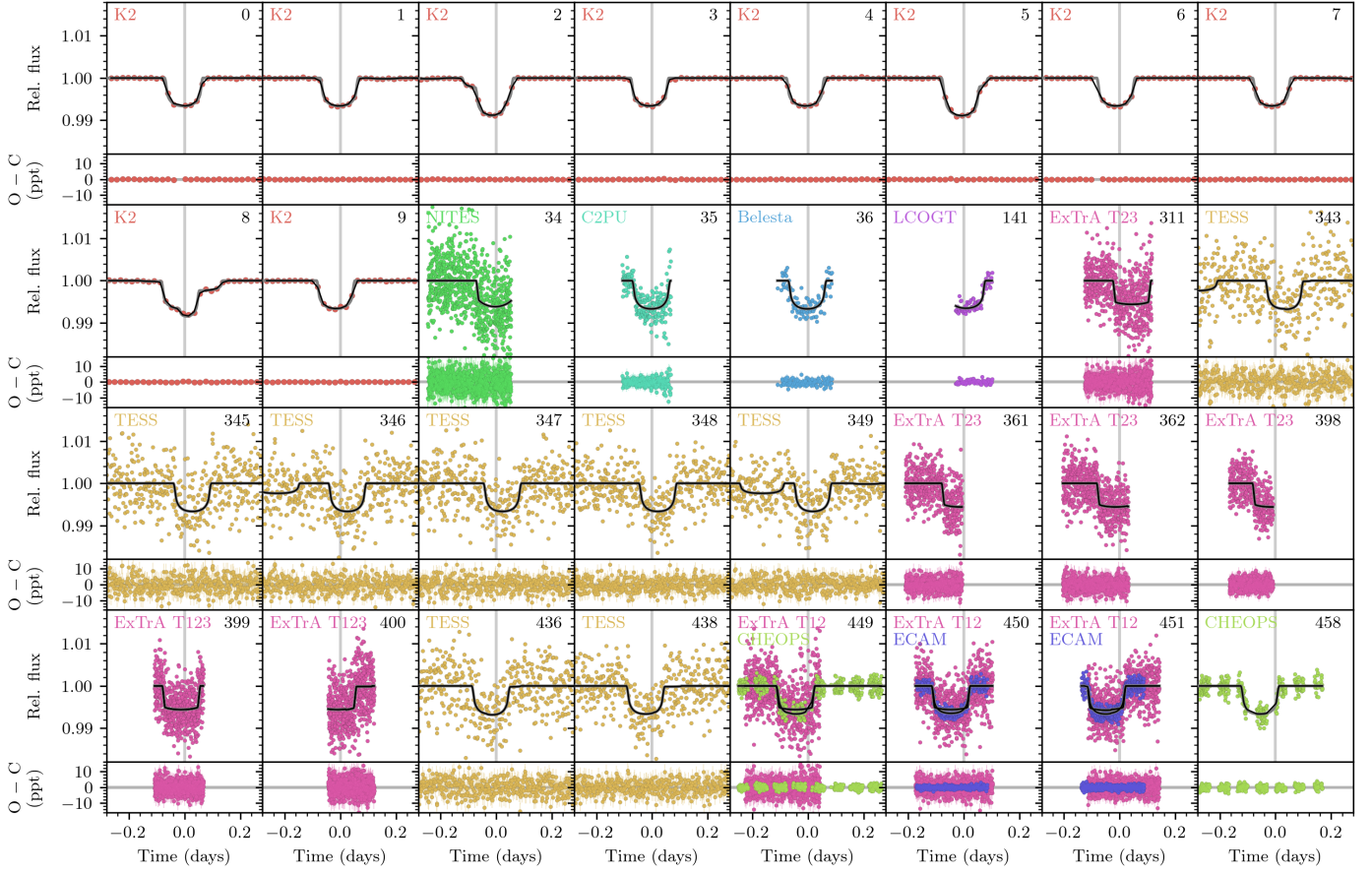


**Fig. A.4.** Same as Fig. A.3, but for K2-19 b.

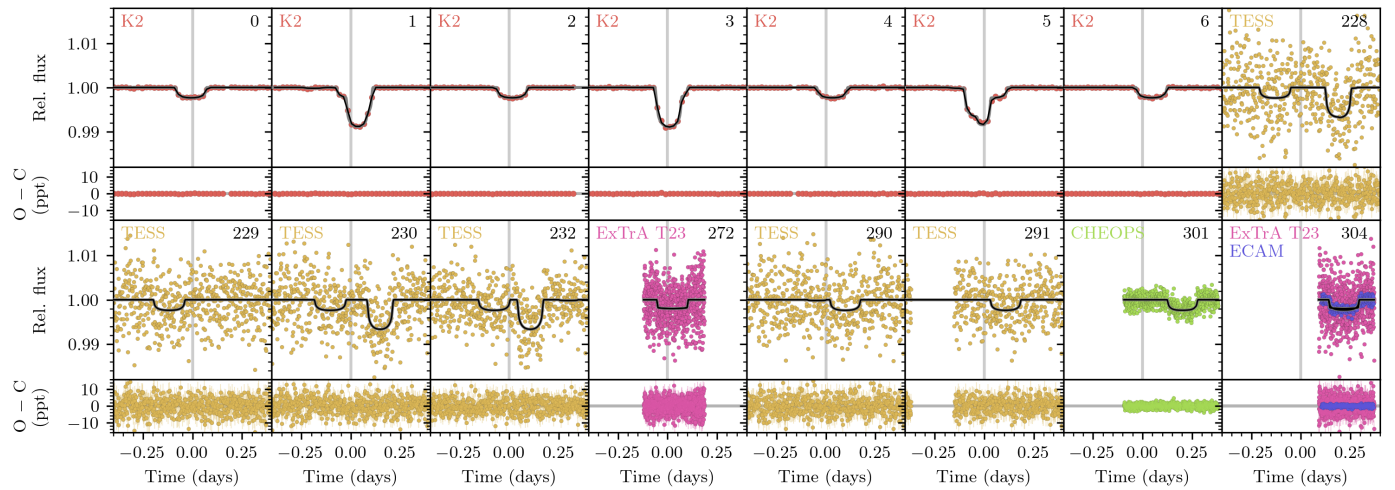


**Fig. A.5.** Same as Fig. A.3, but for K2-19 c.

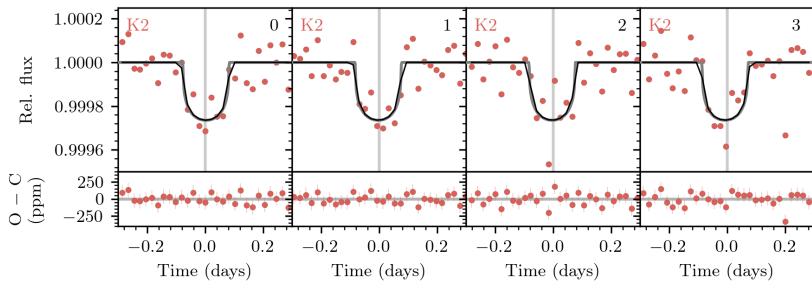


**Fig. A.6.** Same as Fig. A.3, but for K2-19 e.

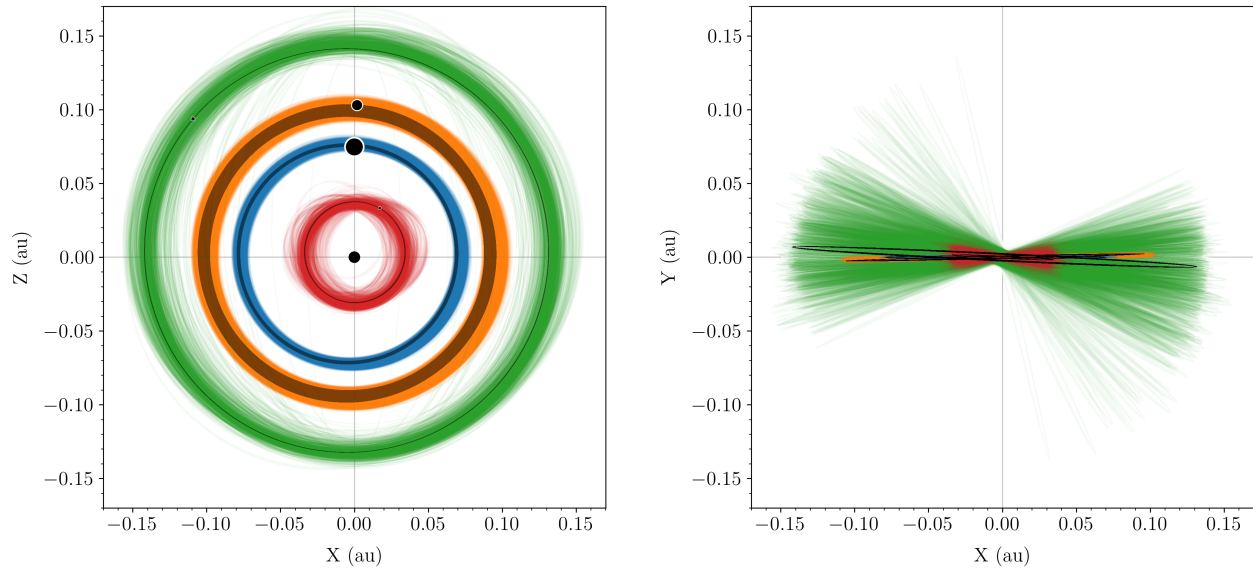


**Fig. A.7.** Orbital projections for the time-span covered by the observations. The origin is the system barycenter, and the orbits are projected in the X-Z plane (left panel, system top view, movement is clockwise, the positive Z-axis points towards the observer) and in the sky plane seen by the observer (X-Y, right panel). A thousand random orbits were drawn from the posterior samples, and the MAP is shown as a gray orbit. In the left panel, the black circles mark the position of the star (size to scale) and the planets (enlarged by a factor of 20) at  $t_{\text{ref}}$  for the MAP.

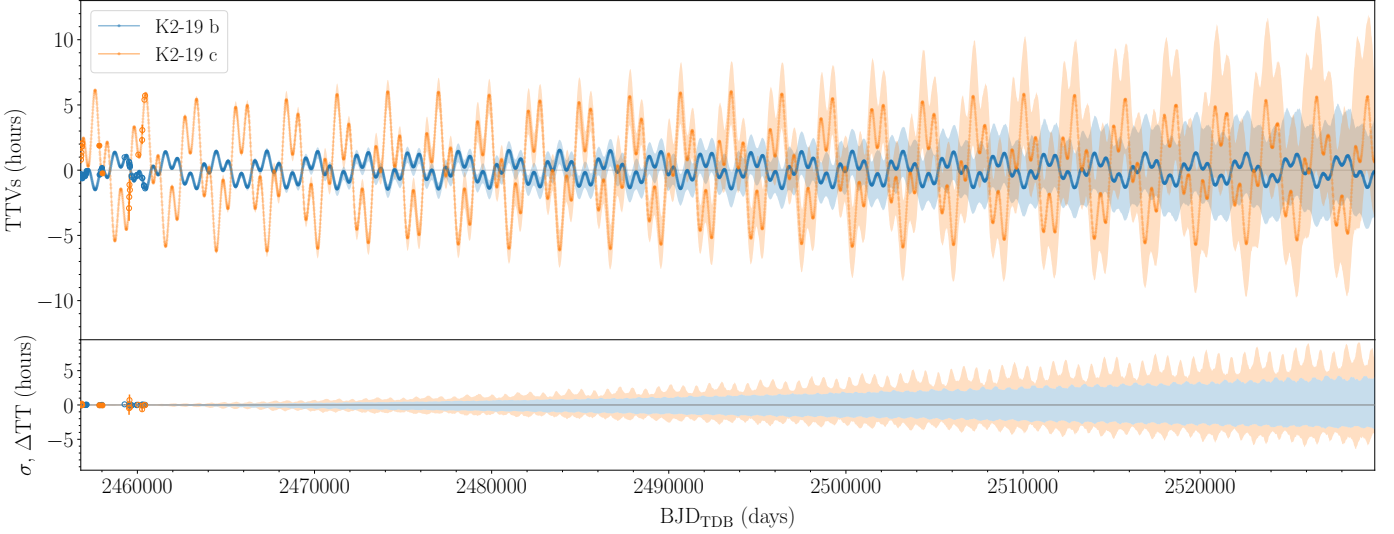


**Fig. A.8.** Same as Fig. 5, but for 200 years from the start of the K2 observations. The linear ephemerides are  $2456813.396578 + 7.92088840 \times \text{Epoch} (\text{BJD}_{\text{TDB}})$ ,  $2456817.239433 + 11.89838594 \times \text{Epoch} (\text{BJD}_{\text{TDB}})$  for planet b and c, respectively

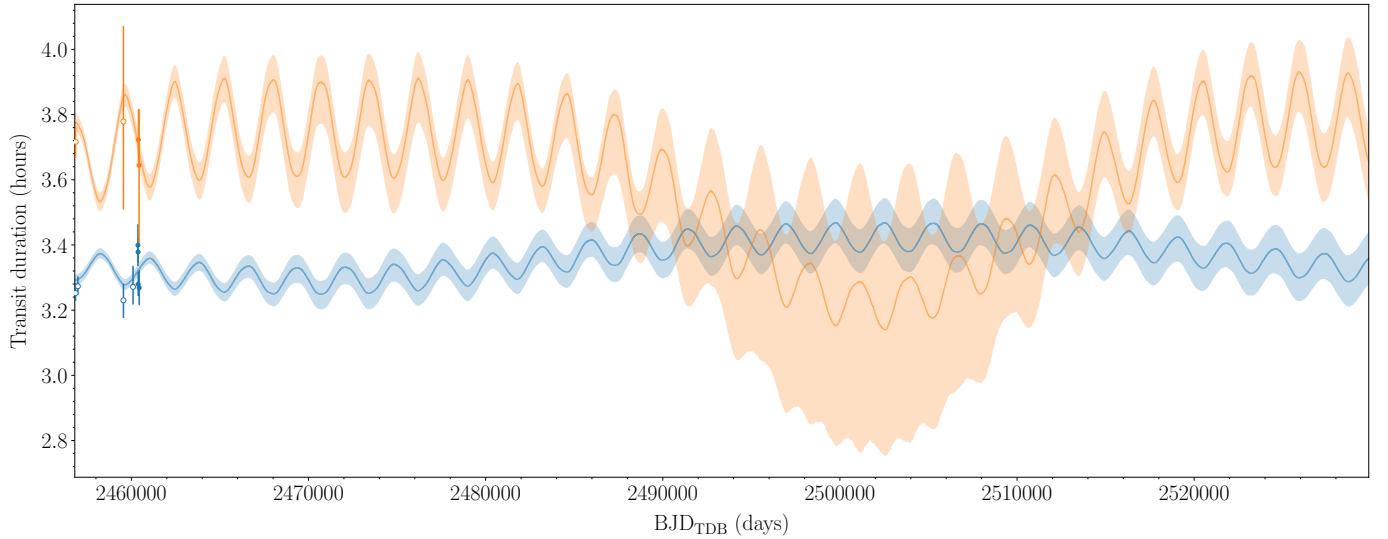


**Fig. A.9.** Same as Fig. 9, but for 200 years from the start of the K2 observations.

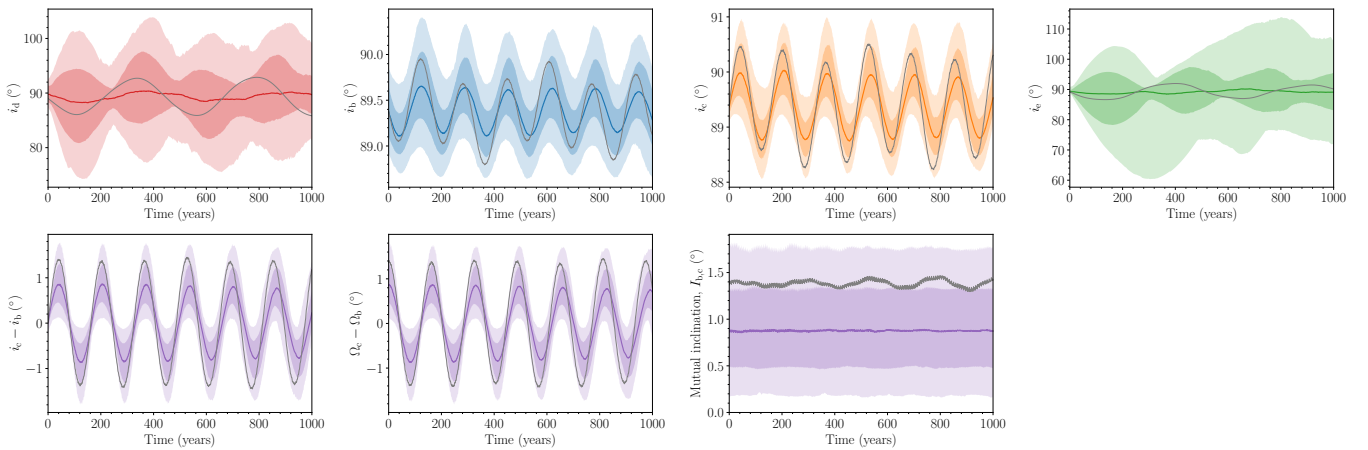


**Fig. A.10.** Orbital inclination (Jacobi) evolution of planets d (first column), b (second column), c (third column), and e (fourth column) from 1000 random samples of the posterior. The 68.3% and 95.4% Bayesian CIs are plotted in different intensities. The solid color curve marks the median of the posterior distribution. The solid gray curves correspond to the parameters of the MAP values. The last line shows some relations of orbital parameters for planets b and c.

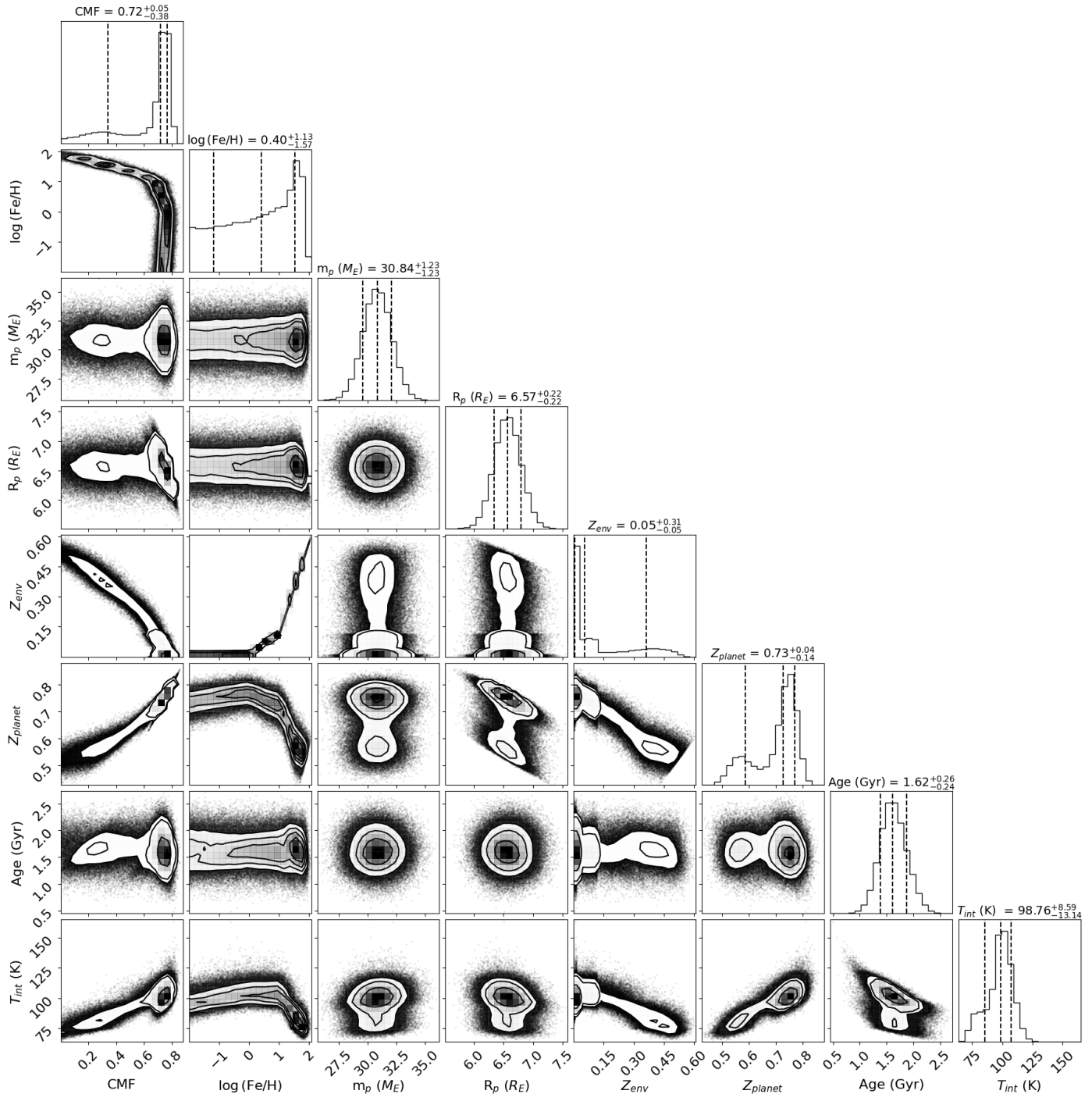


**Fig. A.11.** Two-parameter joint posterior distributions for the most relevant model parameters from the interior retrieval (Sect. 5.7). The 1, 2, and 3 $\sigma$  confidence regions are denoted black contours. The histogram of the marginal distribution for each parameter is shown at the top of each column, except for the parameter on the last line, which is shown at the end of the line.

## Appendix B: Determination of transit times

Transit times of multiple transits observations can be obtained by fitting them simultaneously while assuming constant transit parameters. This approach can obtain more precise values than when each transit is analyzed individually, be less sensitive to stellar activity or instrumental systematics, and it is the safest option if there are partial transits among the observations. Depending on the photometric precision, the transit timing of partial transits presents a degeneracy with the transit duration. This degeneracy is broken if the signal of limb darkening is detected. However, when the transits present TDVs, assuming one transit shape for all transits can bias the derived transit timings. To obtain the transit timings in K2-19, we found a compromise by fitting together groups of transits observed close in time. But we also fit individual transit times for the most precise observations. Simultaneous observations of the same transit were analyzed together. For planet b, we analyzed epochs [311–362] as a group and epochs [398–438] as another group. Epochs 449, 450, 451, and 458 were analyzed individually. For planet c, epochs [228–232] and [290–291] were analyzed as groups, while epochs 272, 301, and 304 were analyzed individually. The partial transit of planet b at epoch 141 (observed with LCOGT), for which the timing presented in Petigura et al. (2020) represents an outlier, was analyzed assuming the transit parameters of K2 observations. The timings of planets d, only detected in K2 observations, were analyzed simultaneously. And the same for planet e candidate (Sect. 4.1). We modeled the datasets with juliet (Espinoza et al. 2019; Kreidberg 2015; Foreman-Mackey et al. 2017; Speagle 2020) using the same noise model as in Sect. 4.2. Table B.1 presents literature and the new transit timings we computed. These timings, derived independently of the assumptions used in the photodynamical modeling (Sect. 4.2), were utilized to validate its results by comparing them with the posterior TTVs (Fig. 5).

**Table B.1.** Transit times of the observations.

Epoch	Posterior median and 68.3% CI [BJD <sub>TDB</sub> ]	Telescope Instrument	Source
<b>Planet d</b>			
0	2456811.426 <sup>+0.015</sup> <sub>-0.010</sub>	K2	This work
1	2456813.945 <sup>+0.010</sup> <sub>-0.010</sub>	K2	This work
2	2456816.433 <sup>+0.018</sup> <sub>-0.014</sub>	K2	This work
3	2456818.965 <sup>+0.015</sup> <sub>-0.014</sub>	K2	This work
4	2456821.468 <sup>+0.017</sup> <sub>-0.012</sub>	K2	This work
5	2456823.990 <sup>+0.019</sup> <sub>-0.019</sub>	K2	This work
6	2456826.490 <sup>+0.014</sup> <sub>-0.018</sub>	K2	This work
7	2456828.954 <sup>+0.011</sup> <sub>-0.011</sub>	K2	This work
8	2456831.486 <sup>+0.011</sup> <sub>-0.011</sub>	K2	This work
9	2456834.007 <sup>+0.015</sup> <sub>-0.011</sub>	K2	This work
10	2456836.5443 <sup>+0.0093</sup> <sub>-0.0084</sub>	K2	This work
11	2456839.025 <sup>+0.013</sup> <sub>-0.013</sub>	K2	This work
12	2456841.514 <sup>+0.015</sup> <sub>-0.015</sub>	K2	This work
13	2456844.041 <sup>+0.015</sup> <sub>-0.016</sub>	K2	This work
14	2456846.582 <sup>+0.018</sup> <sub>-0.018</sub>	K2	This work
16	2456851.523 <sup>+0.016</sup> <sub>-0.015</sub>	K2	This work
17	2456854.069 <sup>+0.014</sup> <sub>-0.016</sub>	K2	This work
18	2456856.571 <sup>+0.016</sup> <sub>-0.016</sub>	K2	This work
19	2456859.082 <sup>+0.014</sup> <sub>-0.015</sub>	K2	This work
20	2456861.6036 <sup>+0.019</sup> <sub>-0.0088</sub>	K2	This work
21	2456864.105 <sup>+0.012</sup> <sub>-0.012</sub>	K2	This work
22	2456866.610 <sup>+0.024</sup> <sub>-0.024</sub>	K2	This work
23	2456869.124 <sup>+0.027</sup> <sub>-0.027</sub>	K2	This work
24	2456871.641 <sup>+0.024</sup> <sub>-0.024</sub>	K2	This work
25	2456874.144 <sup>+0.029</sup> <sub>-0.028</sub>	K2	This work
26	2456876.651 <sup>+0.038</sup> <sub>-0.038</sub>	K2	This work
27	2456879.163 <sup>+0.014</sup> <sub>-0.014</sub>	K2	This work
28	2456881.677 <sup>+0.018</sup> <sub>-0.023</sub>	K2	This work
29	2456884.195 <sup>+0.020</sup> <sub>-0.080</sub>	K2	This work
30	2456886.677 <sup>+0.022</sup> <sub>-0.025</sub>	K2	This work
31	2456889.193 <sup>+0.025</sup> <sub>-0.025</sub>	K2	This work

Epoch	Posterior median and 68.3% CI [BJD <sub>TDB</sub> ]	Telescope	Source
Planet b		Instrument	
0	2456813.38390 ± 0.00056	K2	Barros et al. (2015)
1	2456821.30410 ± 0.00088	K2	Barros et al. (2015)
2	2456829.22194 ± 0.00025	K2	Barros et al. (2015)
3	2456837.13900 ± 0.00064	K2	Barros et al. (2015)
4	2456845.06156 ± 0.00053	K2	Barros et al. (2015)
5	2456852.9794 ± 0.0028	K2	Barros et al. (2015)
6	2456860.90005 ± 0.00079	K2	Barros et al. (2015)
7	2456868.82080 ± 0.00052	K2	Barros et al. (2015)
8	2456876.73856 ± 0.00064	K2	Barros et al. (2015)
9	2456884.65834 ± 0.00080	K2	Barros et al. (2015)
30	2457051.00413 <sup>+0.00218</sup> <sub>-0.00225</sub>	FLWO 1.2 m	Narita et al. (2015)
34	2457082.69550 <sup>+0.00140</sup> <sub>-0.00116</sub>	TRAPPIST-South	Narita et al. (2015)
34	2457082.6892 ± 0.0019	NITES	Barros et al. (2015)
35	2457090.6157 ± 0.0014	1-m C2PU Omicron	Barros et al. (2015)
36	2457098.5368 ± 0.0022	Belesta 82-cm	Barros et al. (2015)
41	2457138.15047 <sup>+0.00145</sup> <sub>-0.00176</sub>	OAO 1.88 m / MuSCAT	Narita et al. (2015)
133	2457866.8604 ± 0.0009	Spitzer	Petigura et al. (2020)
141	2457930.2403 <sup>+0.0015</sup> <sub>-0.0013</sub>	LCOGT-SAAO 1 m	This work
150	2458001.5368 ± 0.0014	Spitzer	Petigura et al. (2020)
311	2459276.8341 <sup>+0.0019</sup> <sub>-0.0020</sub>	ExTrA T23	This work
343	2459530.2882 <sup>+0.0029</sup> <sub>-0.0032</sub>	TESS s45	This work
345	2459546.1269 ± 0.0023	TESS s45	This work
346	2459554.0421 <sup>+0.0021</sup> <sub>-0.0023</sub>	TESS s46	This work
347	2459561.9601 ± 0.0023	TESS s46	This work
348	2459569.8789 <sup>+0.0033</sup> <sub>-0.0029</sub>	TESS s46	This work
349	2459577.7967 <sup>+0.0024</sup> <sub>-0.0025</sub>	TESS s46	This work
361	2459672.8198 <sup>+0.0016</sup> <sub>-0.0017</sub>	ExTrA T23	This work
362	2459680.7365 <sup>+0.0022</sup> <sub>-0.0023</sub>	ExTrA T23	This work
398	2459965.8909 <sup>+0.0021</sup> <sub>-0.0019</sub>	ExTrA T23	This work
399	2459973.8158 <sup>+0.0014</sup> <sub>-0.0017</sub>	ExTrA T123	This work
400	2459981.7360 ± 0.0019	ExTrA T123	This work
436	2460266.8799 <sup>+0.0033</sup> <sub>-0.0032</sub>	TESS s72	This work
438	2460282.7201 <sup>+0.0021</sup> <sub>-0.0022</sub>	TESS s72	This work
449	2460369.8272 ± 0.0012	CHEOPS, ExTrA T12	This work
450	2460377.74640 <sup>+0.00057</sup> <sub>-0.00055</sub>	Euler / ECAM, ExTrA T12	This work
451	2460385.66556 <sup>+0.00070</sup> <sub>-0.00072</sub>	Euler / ECAM, ExTrA T12	This work
458	2460441.10519 <sup>+0.00064</sup> <sub>-0.00066</sub>	CHEOPS	This work
Planet c			
0	2456817.2730 ± 0.0015	K2	Barros et al. (2015)
1	2456829.1835 ± 0.0013	K2	Barros et al. (2015)
2	2456841.0922 ± 0.0014	K2	Barros et al. (2015)
3	2456853.0091 ± 0.0077	K2	Barros et al. (2015)
4	2456864.9083 ± 0.0019	K2	Barros et al. (2015)
5	2456876.8150 ± 0.0014	K2	Barros et al. (2015)
6	2456888.7161 ± 0.0013	K2	Barros et al. (2015)
87	2457852.4774 ± 0.0074	Spitzer	Petigura et al. (2020)
102	2458030.8645 ± 0.0059	Spitzer	Petigura et al. (2020)
228	2459529.950 <sup>+0.019</sup> <sub>-0.040</sub>	TESS s45	This work
229	2459541.884 <sup>+0.015</sup> <sub>-0.022</sub>	TESS s45	This work
230	2459553.822 <sup>+0.034</sup> <sub>-0.017</sub>	TESS s46	This work
232	2459577.602 <sup>+0.027</sup> <sub>-0.018</sub>	TESS s46	This work
272	2460053.6499 <sup>+0.0038</sup> <sub>-0.0028</sub>	ExTrA T23	This work
290	2460267.868 <sup>+0.011</sup> <sub>-0.013</sub>	TESS s72	This work
291	2460279.798 <sup>+0.017</sup> <sub>-0.014</sub>	TESS s72	This work
301	2460398.8787 <sup>+0.0016</sup> <sub>-0.0017</sub>	CHEOPS	This work
304	2460434.5866 <sup>+0.0023</sup> <sub>-0.0022</sub>	Euler / ECAM, ExTrA T23	This work
Candidate planet e			
0	2456812.250 <sup>+0.019</sup> <sub>-0.014</sub>	K2	This work
1	2456832.220 <sup>+0.016</sup> <sub>-0.011</sub>	K2	This work
2	2456852.185 <sup>+0.011</sup> <sub>-0.013</sub>	K2	This work
3	2456872.143 <sup>+0.013</sup> <sub>-0.016</sub>	K2	This work

## Appendix C: TTVs analysis

In this section, we analyze only the transit times of planets b and c (listed in Table B.1). We exclude the partial transit observed by LCOGT, which was analyzed assuming the transit parameters of K2 observations. However, there is a significant time span between both observations. According to the photodynamical modeling, the difference between transits durations is about 6 minutes, so the determination can be biased. For epoch 34 of planet b, for which two timings can be found in the literature, we keep the one by Narita et al. (2015) for the analysis in this section because it is more precise.

To investigate the effect of the coverage of the TTVs signal, we separate the timings into seven datasets: 2014 (only K2 data), 2015 (time span comparable with the photodynamical modeling of Barros et al. 2015), 2017 (this one is equivalent to the modeling of Petigura et al. 2020, in terms of time span), 2021, 2022, 2023, and 2024. For each dataset, only transit times up to the end of the named year were considered.

The model only includes the star and planets b and c. Transit times were modeled as the moments of minimum sky-projected planet–star separation, calculated using Eq. 1 from Deck et al. (2014), with n-body integrations performed in REBOUND, employing WHFast and an integration step of 0.01 days. We fixed the orbital inclination of both planets at  $90^\circ$  (which biases the mutual inclination) and included a jitter term (Gregory 2005) for the dataset of each planet. The eccentricities and argument of pericenter were parameterized using  $\sqrt{e} \cos \omega$  and  $\sqrt{e} \sin \omega$ . We used uniform priors for all parameters. The joint posterior distribution was sampled using emcee (Goodman & Weare 2010; Foreman-Mackey et al. 2013). The marginal posterior distribution of selected parameters are shown in Fig. C.1, and the TTVs plots are in Fig. C.2.

Nascimbeni et al. (2024) asserts that the period modulation of the TTV needs to be fully mapped to avoid degeneracy in the dynamical retrieval. When comparing the 2015 dataset to Barros et al. (2015), the photodynamical modeling appears to be less impacted by this degeneracy than the TTV analysis. The distinction between modeling just transit times and employing photodynamical modeling is more noticeable in 2015, which has less coverage of the TTV signal (see Fig. C.3 and the 2015 panel in Fig. C.2), than in 2024 (see Fig. 5 and the 2024 panel in Fig. C.2). The posteriors from the photodynamical modeling (Sect. 4.2) are slightly more precise than those from the transit-time analysis of the 2024 dataset for the shared parameters, although both agree within  $1\sigma$ . With the exception of the 2015 dataset (and 2024, which uses all available data), the remaining datasets predict future observed transits within  $1.6\sigma$  for planet b and within  $2.6\sigma$  for planet c (Fig. C.2).

We repeated the analysis of the 2017 dataset, including the discrepant LCOGT transit timing from Petigura et al. (2020), to investigate if it could be responsible for their retrieved higher eccentricities and poor transit timing forecasts (Fig. C.4). The TTV model is able to fit the discrepant timing and produces transit timing forecasts similar to those of the 2017 dataset without the LCOGT timing (see Figs. C.2 and C.5). However, the posterior eccentricities exhibit notable differences (see Fig. C.1). The posteriors for the dataset that includes the LCOGT transit timing from Petigura et al. (2020) are narrower and centered around a higher eccentricity. Therefore, this discrepant timing could be at least partially responsible for the higher eccentricity value found by these authors. The reasoning is as follows: The Petigura et al. (2020) analysis used a photodynamical modeling for the K2 data and modeled only the transit timings for the other

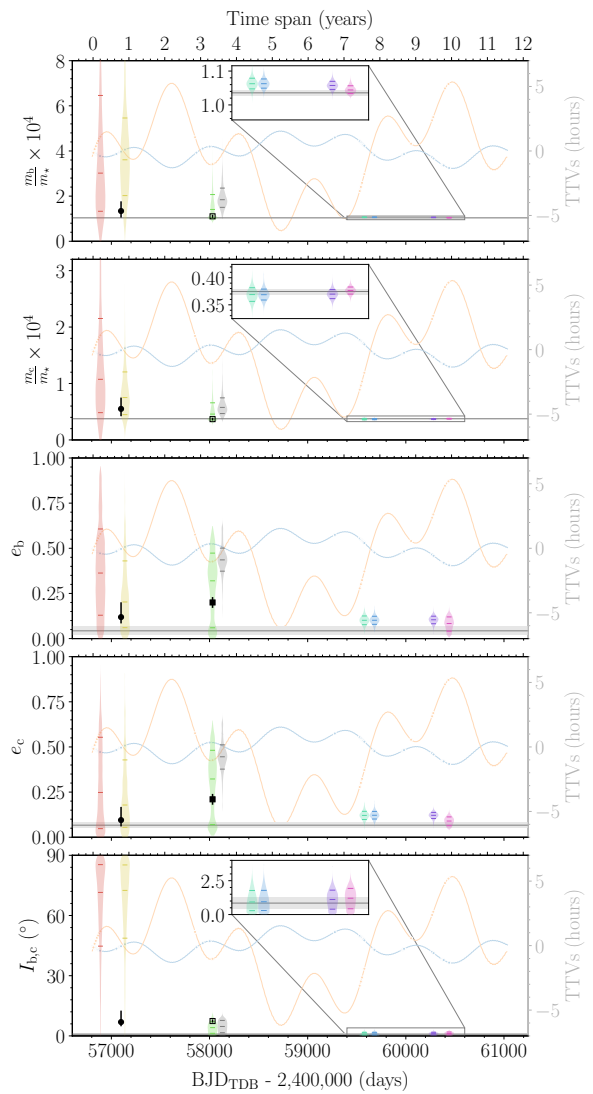


**Fig. C.1.** Comparison of the marginal posterior distribution (violins) of selected parameters (orbital parameters are at  $t_{\text{ref}}$ ) for the analysis of the transit times with different time spans. Violins are positioned at the time of the last observation considered in the analysis and horizontal ticks inside them marks the median and 68.3% CI of the marginal posterior distribution. The gray violins corresponds to the 2017 dataset using the LCOGT timing from Petigura et al. (2020) and are offset to the right for clarity. The horizontal line and gray band represent the median and 68.3% CI of the marginal posterior distribution from the photodynamical analysis of Sect. 4.2. The insets provide a zoomed view of the last four transit timing analyses. Results from the photodynamical analysis of Barros et al. (2015) are shown with black circle error bars, and those of Petigura et al. (2020) with black square error bars (open squares correspond to derived values assuming normal distributions for the quoted parameters, and thus do not account for correlations between them). In the background, the median posterior TTVs for planets b (light blue) and c (light orange) from the photodynamical analysis of Sect. 4.2 are shown, and dots mark the observed transits.

datasets. The discrepant LCOGT transit timing from Petigura et al. (2020) pushes to moderate eccentricity, but the photodynamical modeling, which has an additional constrain on the eccentricity from the transit shape, pushes to lower eccentricities. In the end, their posterior converges to an intermediate value between these two. If this is correct, performing photodynamical modeling of all datasets would have avoided this problem.

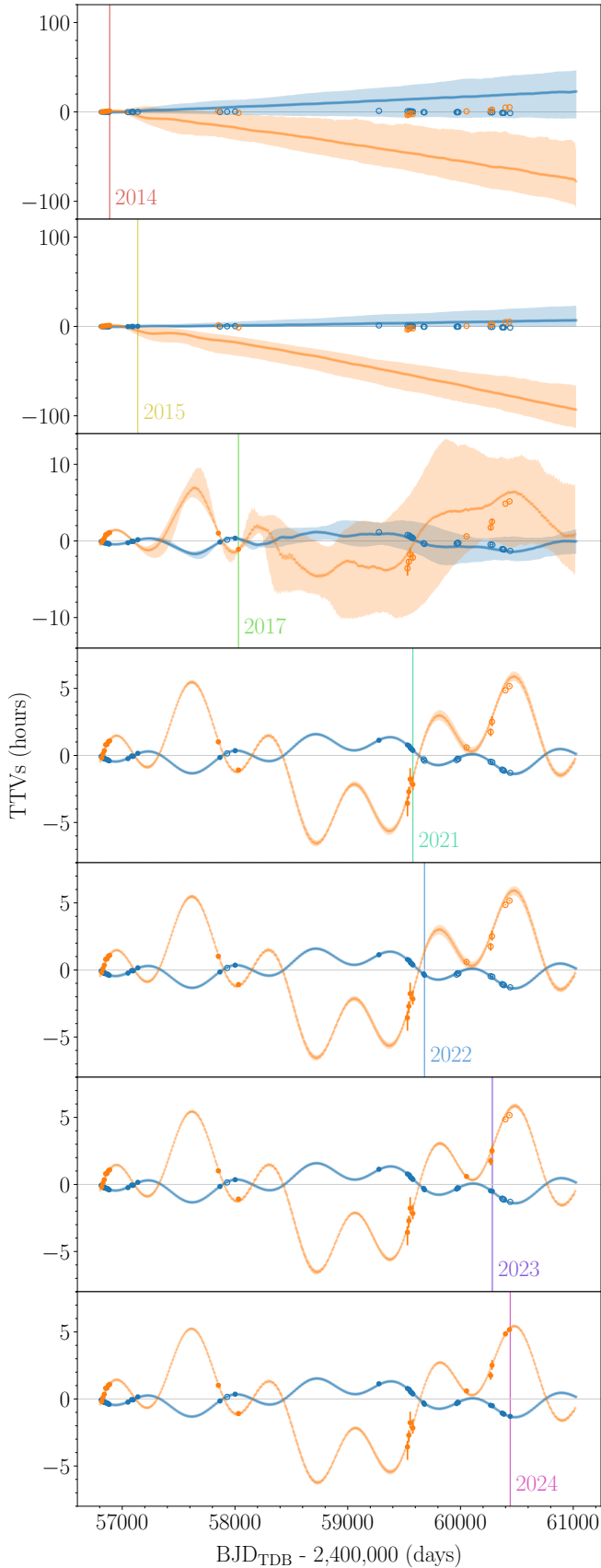


**Fig. C.2.** Same as Fig. 5, but for the analysis using only transit times up to the end of the labeled year and only planets b and c in the model. The labeled vertical line (the color code is the same as in Fig. C.1) marks the last observation modeled. Filled circles represent the times used in the analysis of each of the panels, while open circles indicate observations that are not used.

Article number, page 22 of 22

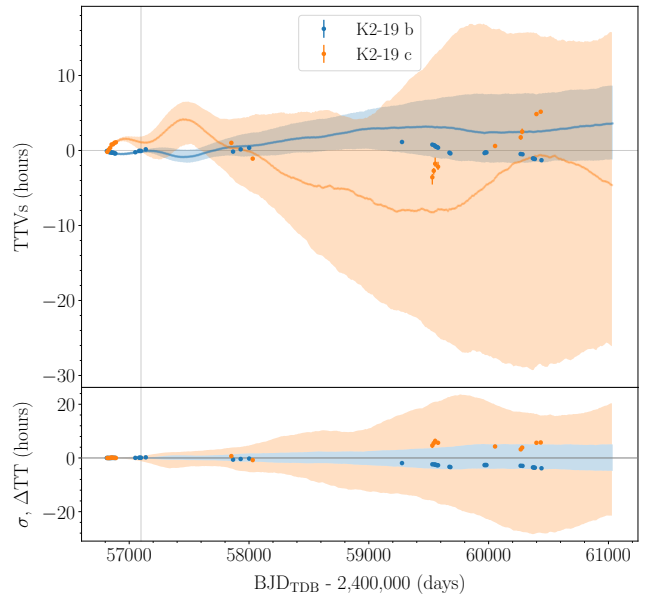


**Fig. C.3.** Same as Fig. 5 but for Barros et al. (2015) TTVs posterior (blue and orange bands) compared with observations (error bars, Table B.1). The vertical gray line marks the last observation modeled.

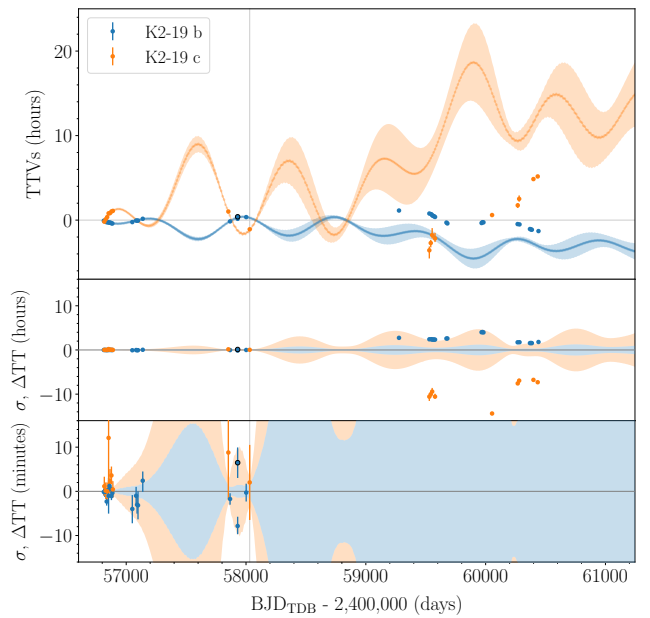


**Fig. C.4.** Same as Fig. C.3 but for Petigura et al. (2020). Their 141 epoch of planet b timing is the error bar encircled in black.

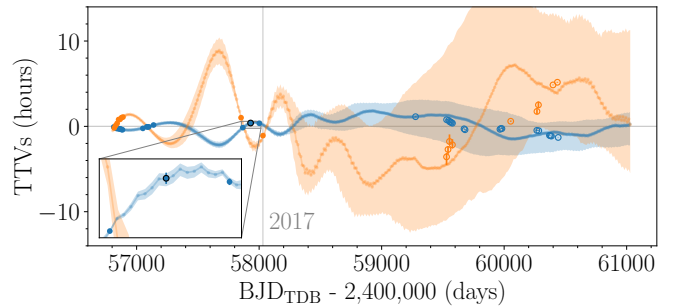


**Fig. C.5.** Same as Fig. C.2 for the 2017 dataset with the 141 epoch of planet b timing from Petigura et al. (2020) observed with LCOGT (error bar encircled in black).